1

Structures of the Cyanobacterial Phycobilisome

Paul V. Sauer[*,1,2] (0000-0001-7204-5863), Maria Agustina Dominguez-Martin[*,3,4,5] (0000-0002-3500-2052), Henning Kirst[3,4] (0000-0002-6982-4345), Markus Sutter[3,4,5] (0000-0001-6290-4820), David Bina[6,7] (0000-0002-9259-4218), Basil J. Greber[1,4,8] (0000-0001-9379-7159), Eva Nogales[1,2,4,9] (0000-0001-9816-3681), Tomáš Polívka[6] (0000-0002-6176-0420) & Cheryl A. Kerfeld[3,4,5,10 (#)] (0000-0002- 9977-8482)

[1] QB3 Institute, University of California, Berkeley, CA, USA

[2] Howard Hughes Medical Institute, University of California, Berkeley, CA, USA

[3] Environmental Genomics and Systems Biology Division, Lawrence Berkeley National Laboratory, Berkeley, CA 94720, USA.

[4] Molecular Biophysics and Integrated Bioimaging Division, Lawrence Berkeley National Laboratory, Berkeley, CA 94720, USA.

[5] MSU-DOE Plant Research Laboratory, Michigan State University, East Lansing, MI 48824, USA.

[6] Faculty of Science, University of South Bohemia, Ceske Budejovice, Czech Republic

[7] Biology Centre of the Czech Academy of Sciences, Ceske Budejovice, Czech Republic

[8] Present address: Division of Structural Biology, Institute of Cancer Research, London, UK

[9] Department of Molecular and Cellular Biology, University of California, Berkeley, CA, USA.

[10] Department of Biochemistry and Molecular Biology, Michigan State University, East Lansing, MI 48824, USA

[*] These authors contributed equally to this work.

[#] Address correspondence to: ckerfeld@lbl.gov

The author responsible for distribution of materials integral to the findings presented in this article is: Cheryl A. Kerfeld (ckerfeld@lbl.gov).

Abstract

29 The phycobilisome is an elaborate antenna that is responsible for light-harvesting in cyanobacteria and

30 red-algae. This large macromolecular complex captures incident sunlight and transfers the energy via

31 a network of pigment molecules called bilins to the photosynthetic reaction centers. The phycobilisome

32 of the model organism *Synechocystis* PCC 6803 consists of a core to which six rods are attached but

33 its detailed molecular architecture and regulation in response to environmental conditions is not well

34 understood. Here we present cryo-electron microscopy structures of the 6.2 MDa phycobilisome from

35 *Synechocystis* PCC 6803 resolved at 2.1 Å (rods) to 2.7 Å (core), revealing three distinct

36 conformations, two previously unknown. We found that two of the rods are mobile and can switch

37 conformation within the complex, revealing a layer of regulation not described previously. In addition,

38 we found a novel linker protein in the structure, that may represent a long-sought subunit that tethers

39 the phycobilisome to the thylakoid membrane. Finally, we show how excitation energy is transferred

40 within the phycobilisome and correlate our structures with known spectroscopic properties. Together,

41 our results provide detailed insights into the biophysical underpinnings of cyanobacterial light

42 harvesting and lay the foundation for bioengineering of future phycobilisome variants and artificial

43 light harvesting systems.

44

45

46

47

48

49

50

51

52

Structures of the Cyanobacterial Phycobilisome

53   Cyanobacteria are the most abundant and ecophysiologically diverse primary producers on Earth.

54   Oxygenic photosynthesis is an ancient cyanobacterial innovation that allowed complex life to emerge[1],

55   and today these organisms are being established as platforms for green biotechnologies[2].

56   Cyanobacterial phycobilisomes (PBSs)[3-5] are massive pigment-protein complexes that can constitute

57   up to half of the soluble protein content of the cell[6]. The two major PBS substructures, the core and

58   the rod, are composed of phycobiliproteins, and colorless linker proteins (LPs)[7]. Phycobilin pigments

59   are covalently bound to the phycobiliproteins[8-14], which assemble into disc-like trimers $(\alpha\beta)_3$ or

60   hexamers $(\alpha\beta)_6$. These discs are chained together in the rods and core cylinders by LPs and organized

61   into a complete PBS[15-17]. The association of pigments with protein tunes the pigments' energetic

62   properties to establish an energy cascade to the photosynthetic reaction centers that is both extremely

63   fast and highly efficient (ca. 95%)[18,19]. Four morphological types of PBS are known:

64   hemiellipsoidal[16,20,21], block-type[15], hemidiscoidal[10,22-25] and bundle-type[26]. *Synechocystis* PCC 6803

65   is the primary model system for molecular and spectroscopic studies [27] containing the most widespread

66   type of PBS, the hemidiscoidal[8,22,25,28,29], which is also the evolutionary antecedent of all types of

67   PBS[15]. We report three cryo-electron microscopy (cryo-EM) structures of the 6.2 MDa PBS from

68   *Synechocystis* PCC 6803, representing distinct conformers of rod arrangements: the canonical 'up-up'

69   (2.7 Å), and two previously undescribed, 'up-down' (2.8 Å), and 'down-down' (3.5 Å) conformations.

70   We also describe the structure of all the linkers, one of them previously unknown, the arrangement of

71   all bilins, and elucidate the likely energy transfer pathway.


72   **Structural overview**

73   Purified and intact PBS complex was biotinylated and subjected to cryo-EM using streptavidin affinity

74   grids[30] to reduce preferential particle orientations and to increase stability (Methods, Extended Data

75   Fig. 1, Extended Data Table 1, 2). We determined the structure of three distinct PBS conformations at

76   resolutions ranging from 2.7 to 3.5 Å for the entire complexes, enabling us to build all pigments and

77 protein chains (Fig. 1, Extended Data Fig. 2, 3, and Extended Data Table 3). As previously reported[22],

78 the rods are flexible in nature and therefore appear smeared in the reconstructions. Therefore, the rods

79 were processed and reconstructed independently, yielding a resolution of 2.1 Å. The rods cannot be

80 further sorted into distinct classes, suggesting that all rods within one complex are identical (Extended

81 Data Fig. 2c).

82 The PBS core consists of three cylinders, a top cylinder (T) stacked on top of two basal cylinders (B1,

83 B2) (Fig. 1, Extended Data Fig. 4). Each of the two B cylinders have one rod attached while four rods

84 are attached to the T cylinder. The core consists of 80 polypeptide chains and 72 phycocyanobilins

85 (PCB), and each rod contains 40 protein subunits and 54 PCBs, adding up to a total of 320 proteins

86 and 396 bilin molecules that amount to a molecular weight of 6.2 MDa. Extended Data Figure 4 and

87 Extended Data Table 1 provide an inventory of the subunits, their component protein family (pfam)

88 domains and functional characteristics.

Structures of the Cyanobacterial Phycobilisome
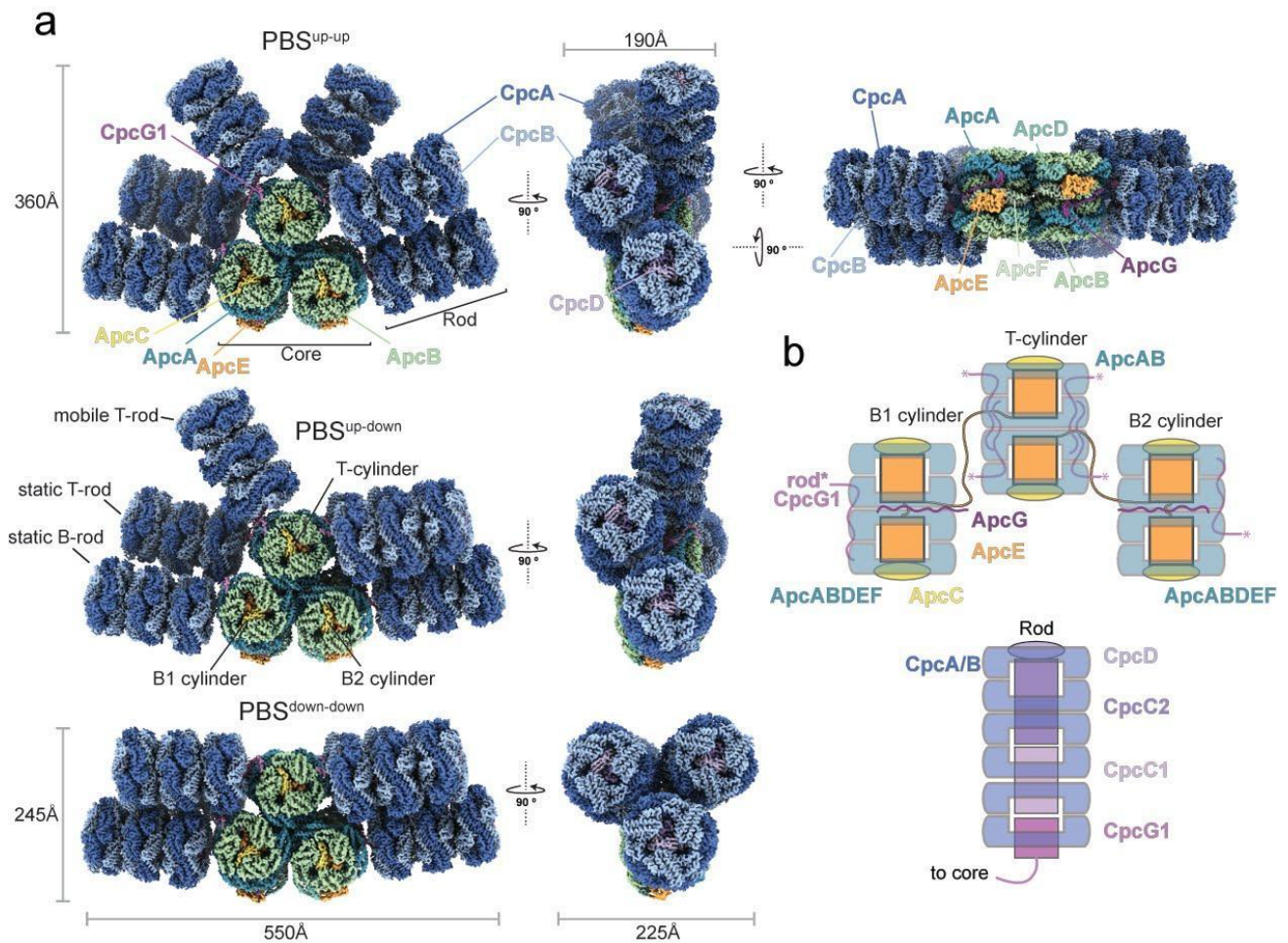
Figure 1: Structural characterization of the phycobilisome from Synechocystis PCC 6803. *a, Composite cryo-EM density maps representing the three PBS conformations: Up-up (top), up-down (middle), down-down (bottom). Individual maps and resolution for the three conformations and the rod can be found in Extended Data Fig. 2. **b**, Schematic overview of PBS connectivity and subunit arrangement of the core (top) and the rods (bottom).*

In contrast to earlier studies, our structures include three different, major rod conformations; two have not been visualized before. They are distinguished by alternate positioning of two of the four T rods (hence referred to as mobile T rods, as opposed to the static T rods). In the 'up-up' conformation, both mobile rods are tilted upwards, corresponding to the canonical hemidiscoidal PBS. Two previously unreported conformers were also present: the 'up-down' conformation, where one of the mobile rods moved downwards to assume a position parallel to the other rods and the 'down-down' conformation, in which all the T cylinder rods are in a down position, reducing the 'height' of the complex by more than 100 Å and giving the PBS a more compact profile (Fig. 1a).

5

102 **Linker architecture and identification of a new linker component, ApcG**

103 Both the core and the rods contain linker proteins in their central cavities that provide scaffolding and

104 organize the arrangement of the Apc and Cpc subunits, thereby ensuring the proper orientation and

105 spacing of the pigments (Fig. 1b, 2a). Central to the organization are two copies of ApcE (Fig. 2a, b,

106 Extended Data Fig. 5a) which form the major scaffold for the core by connecting the bottom with the

107 top cylinders[15-17]. The PB loop (residues 87-129) is disordered and could not be modeled, but all other

108 ApcE domains are well resolved. The three cylinders are 'capped' by six copies of ApcC that interact

109 with ApcE (Fig. 2a, Extended Data Fig. 5b).

Structures of the Cyanobacterial Phycobilisome
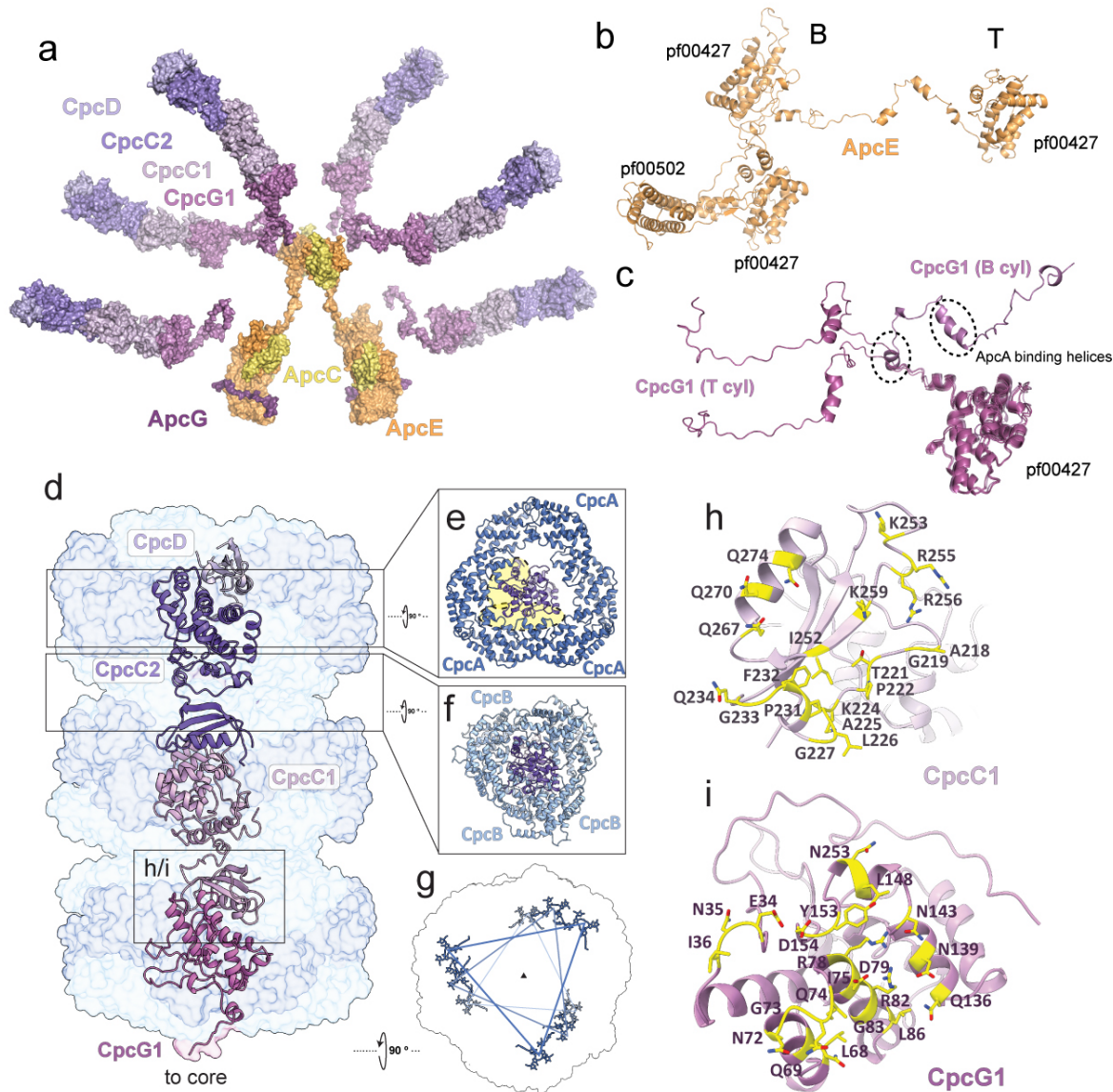
Figure 2: Core and rod linkers. *a, Surface representation of the linker skeleton of the entire PBS. b, ApcE with its constituent domains pf00502 and pf00427. c, CpcG1 linker conformations from top (T) and bottom (B) cylinders in the up-up conformation. d, Linker proteins within a rod. CpcC1/2 contain a pf00427 and pf01383 domain, CpcD only a pf01383 domain e, Interface of CpcC2 with CpcA proteins. Predominant contacts between the linker and CpcA proteins are highlighted in yellow. f, CpcC1/2 interact more closely with CpcB than CpcA. g, Bilin arrangement within the rod showing spiraling pattern. h and i, CpcC1 and CpcG1 amino acids interfaces along the long axis of the rod highlighted in yellow.*

In the rods, there are four linker proteins (Fig. 2 a, d). CpcG1 is located at the core-proximal side. Its 60 residue C-terminal extension attaches it to the PBS core (Figure 2 c, d, Extended Data Fig. 5c). The homologues CpcC1 and CpcC2 form the bulk of the interior of the rods (Fig. 2d, Extended Data Fig.

120   5 d). The interdomain linker of CpcC1 is 15 residues longer than in CpcC2, allowing for a 70º rotation

121   of the pf01383 domain of CpcC1 compared to CpcC2 (Extended Data Fig. 5d). This results in an

122   apparent 10º rotation between each CpcA/B hexamer (Fig. 2g). Even though all linker proteins within

123   the rod employ the same two domains to connect to one another, differences in the binding interface

124   of each domain pair define a unique architecture for the correct assembly of the entire rod (Fig. 2 h, i,

125   Extended Data Fig. 5 e-g).

126

127   A previously unknown linker protein (*sll1873*) was discovered in the cryo-EM density and identified

128   by mass spectrometry (Fig. 3a, Extended Data Table 2). We denote it ApcG or L_{C10} in continuation of

129   the established nomenclature. It is found only on the bottom two cylinders extending toward the

130   membrane-facing side. An HMM search reveals that homologues are found in about 80% of

131   cyanobacterial genomes. ApcG contains two conserved sequence motifs including a short helix that

132   binds in a groove on ApcA like CpcG1 (Fig. 3b, Extended Data Fig. 5b). The highly conserved residue

133   R100 of ApcG directly contacts the PCB of ApcA in the bottom cylinder, suggesting that it may

134   finetune its spectroscopic properties. It has previously been suggested that the PBS interacts with lipid

135   head groups[31]; ApcG could mediate this interaction through its positively charged linker region (Fig.

136   3b). Given its location close to the terminal emitters and the membrane, we propose that ApcG likely

137   plays a key role in PBS localization and energy transfer to PSII.

138   **Terminal emitters**

139   At the membrane facing side of the PBS, the terminal chromophores of ApcD and ApcE are

140   responsible for transferring the absorbed energy to the reaction centers (Fig. 3c, Extended Data Fig.

141   4). ApcF has been shown to play a crucial role in energy migration to ApcE and also to impact state

142   transitions[32,33]. The center-to-center distance between the PCBs of ApcE and ApcF is 23 Å, and 35 Å

143   between the PCBs of ApcD and ApcF (Fig. 3d). While these distances fall well within the range of

144   other PCB distances, their local environments are likely responsible for the observed shift in

145   fluorescence emission of ApcE and ApcF to 680 nm (as opposed to 660 nm for ApcA). Rigid body

146   docking of our structure into a negative stain map of the related *Anabaena sp.* PBS bound to PSII[25]

147   suggests that the closest inter-pigment distance between the PBS and PSII might be as large as ~50 Å

148   (Fig. 3e). The requirement to spectroscopically bridge such a distance might be one of the drivers for

149   the diversification of ApcD, E and F around the terminal chromophores of the PBS and leading to their

150   unique properties.
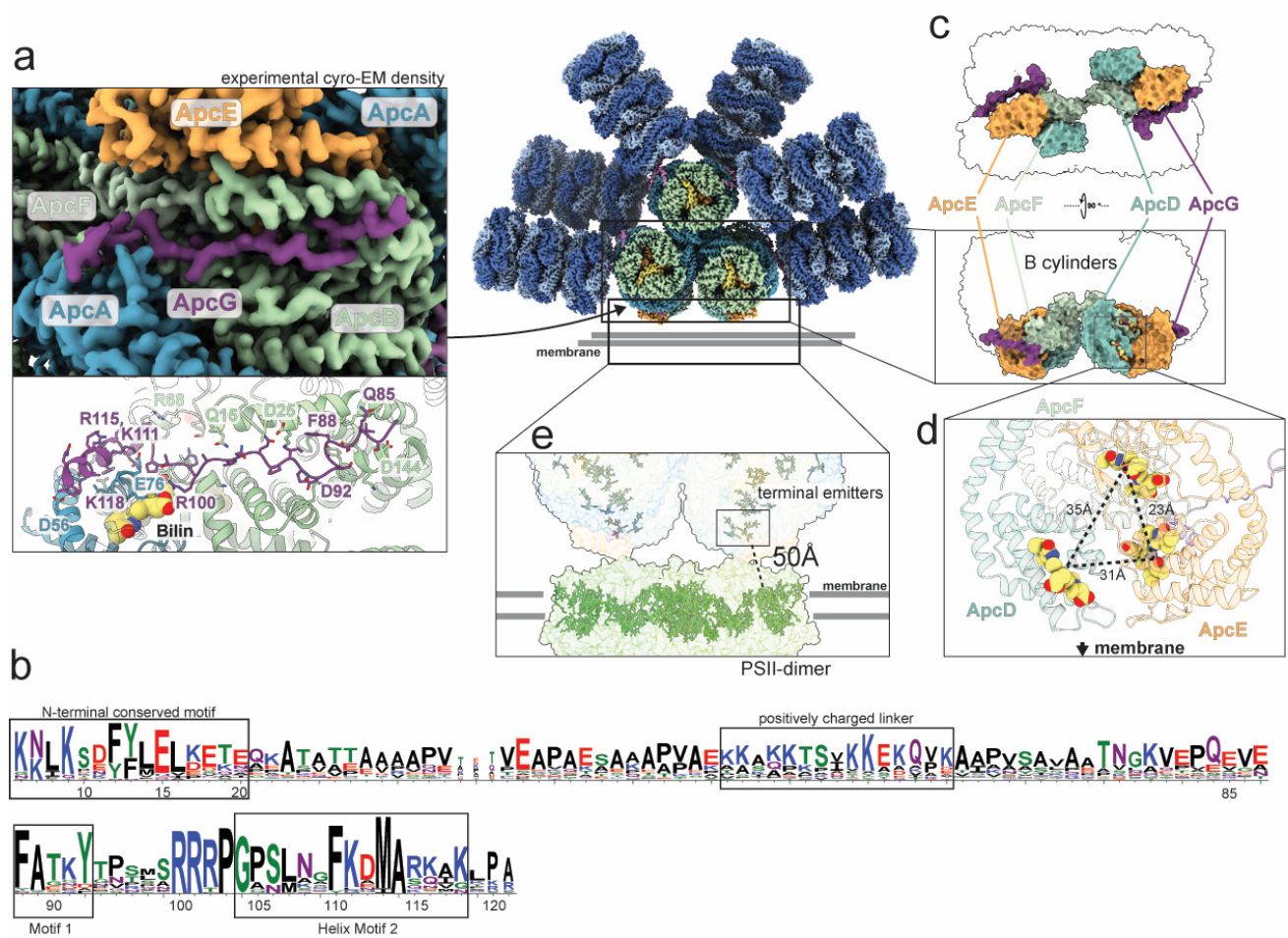
151

152   **Figure 3: A newly identified linker ApcG and Terminal emitters. a**, *Position and interaction of ApcG within the PBS.* **b**,

153   *Sequence conservation logo of ApcG homologs. The numbers refer to residue positions in Synechocystis PCC 6803 ApcG.*

154   *ApcG contains three conserved sequence motifs including a short helix that binds in a central groove of ApcA like CpcG1.*

155   **c**, *Position and orientation of the subunits ApcD, ApcE, ApcF and ApcG within the core of the PBS. Only the*

9

Structures of the Cyanobacterial Phycobilisome

156 *phycobiliprotein domain of ApcE is rendered. **d**, Orientation and distances of the PCBs of ApcD, ApcE and ApcF. **e**, Rigid*

157 *body modelling of our PBS core structure onto PSII, using EMDB 2822 as a reference.*

Core-rod linker architecture and conformational switching

159 Rod attachment is mediated by CpcG1, which protrudes from the central cavity of each rod and latches

160 onto the surface of the core cylinders. The PBS core accommodates the CpcG1 linkers through a

161 network of grooves that span the surfaces of ApcA and ApcB and which can be divided into central

162 and lateral grooves (Fig. 4a, Extended Data Figure 6a). Unlike the algal PBS complexes, grooves from

163 separate discs can align to create a curving binding path for the CpcG1 linkers (Figure 4a).
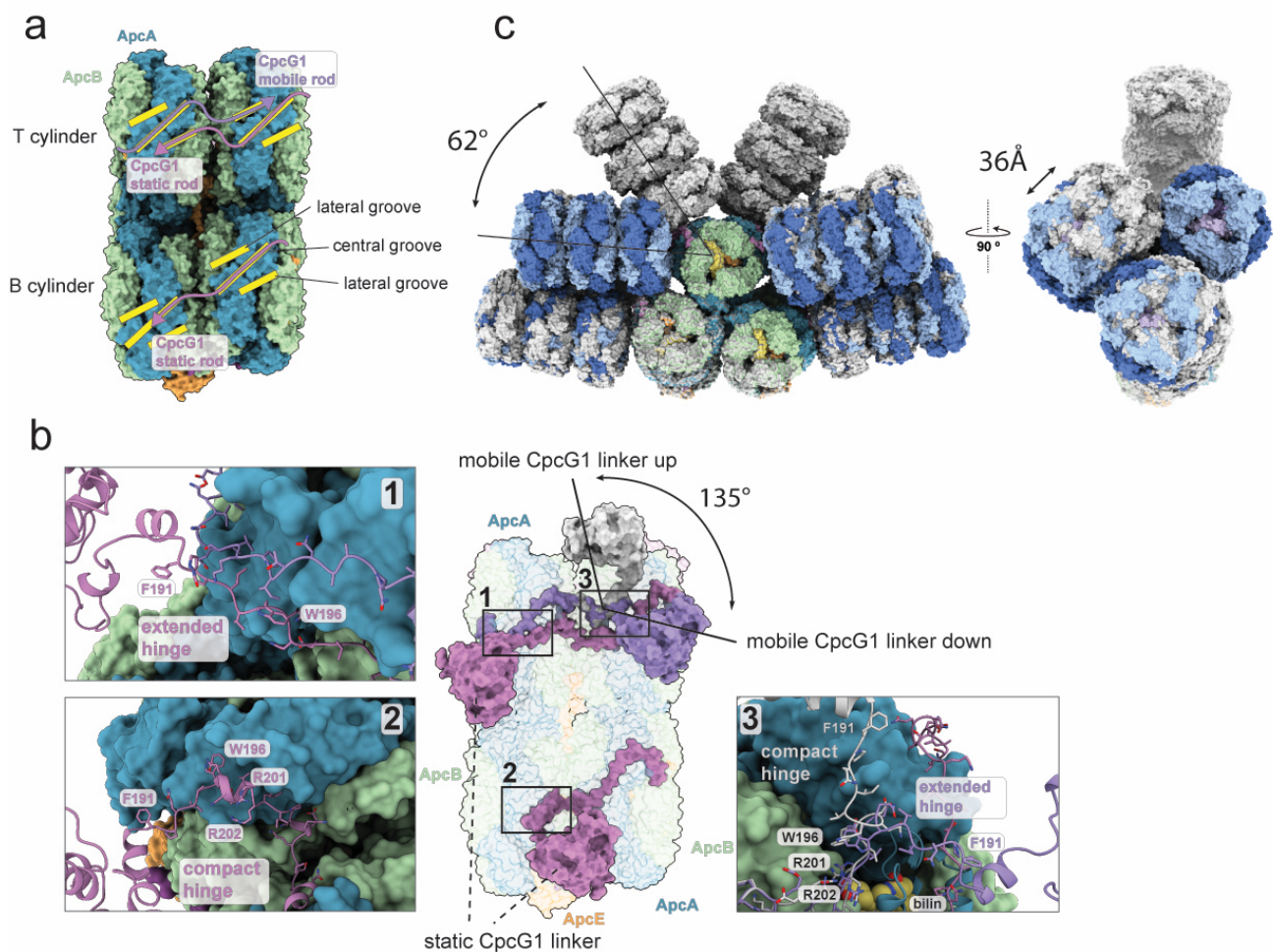
*Figure 4: Structural basis for conformational switching. **a** Side view of the PBS core omitting the rods showing the groove network that organizes CpcG1 linker attachment. **b**, Same side view of the PBS core emphasizing the CpcG1 position. Center panel shows an overview while numbered insets show the different hinge conformations. Near the hinge of the*

10

Structures of the Cyanobacterial Phycobilisome

168   *mobile rod is a PCB molecule that is contacted by R201 of CpcG1.* **c,** *Superimposition of PBS$^{down-down}$ (in color) and PBS^{up-}*

169   *^{up} (light grey) showing the large conformational differences between the two.*

170   The conformations of the CpcG1 linkers correlate within the three rod (Fig. 4b). When comparing the

171   linkers of the top and bottom static rods it is apparent that the linker can adopt one of two different

172   conformations: extended or compact. In the compact state, a conserved six amino acid region (W196-

173   R201), which we define as the 'hinge' forms a small coil or helix that changes the local geometry of

174   the linker relative to the extended state (Fig. 2c, 4b). Of the two static rods, the hinge of the upper rod

175   adopts the extended conformation, while the hinge of the lower rod is in the compact conformation

176   (Fig 4b). As a consequence of this conformational difference, the globular domain of the lower CpcG1

177   is rotated with respect to the globular domain of the upper CpcG1. This rotation is locked in place only

178   for the static rods, the mobile rod however can toggle between these two states which are determined

179   by the conformation of the hinge. Superposing the position of CpcG1 of the mobile rod in its 'down'

180   conformation with its own 'up' conformation reveals that the movement of the mobile rod between

181   'down' and 'up' corresponds to the conformational change of the linker between compact and

182   extended. As a result, the globular CpcG1 domain along with the entire rod rotates by 135º around its

183   long axis when swinging from 'down' to 'up' (Fig. 4b). Most importantly, this switch is accommodated

184   by a 62º upwards swing of the entire rod, which is the most striking difference between the 'down'

185   and 'up' conformations (Fig. 4c). A similar conformational change from the mobile rod to the static

186   rods is precluded because it would result in a clash of the static rods. The bottom static rod would

187   swing upwards while the upper static rod would swing downwards. This mutual blockade alone is

188   sufficient to explain the static nature of these two rods.

189   The mobile rod is held in place in its 'down' position through interactions with its static rod neighbor.

190   Two Cpc(αβ)$_6$ hexamers proximal to the PBS core interact through a salt bridge that is formed between

191   R150 of one of the CpcB's in the mobile rod and E131 of one of the CpcA's in the static rod (Extended

192   Data Fig. 6b).

193 The superposition of 'down' and 'up' conformations also reveals that the upper static rod experiences

194 a 36 Å lateral displacement when the mobile rod is down but relaxes into its central position once the

195 mobile rod swings upwards (Fig. 4c). Once in the central position, the static rod obstructs the

196 downward movement of the mobile rod and stabilizes this conformation. Hence, in every case the

197 mobile rod needs to overcome an energy barrier to move either direction.

198 **Energy transfer pathways in the different PBS conformations**

199 To better understand the impact of the different conformations we computationally modeled the energy

200 transfer within the phycobilisome based on our structural data. We assume energy transfer in the limit

201 of Förster theory using a dipole-dipole approximation for inter-pigment couplings. The map of energy

202 transfer rates for the PBS in the up-up conformation is shown in Fig. 5, demonstrating a robust system,

203 in which excitation of essentially any pigment directs the excitation quickly to the terminal emitters.

204 It also shows that the bottleneck is the rod-to-core energy transfer, as suggested by global fitting

205 models of time-resolved fluorescence data[34]. Energy transfer between the pigments in the core, both

206 within and between the cylinders, is more efficient than rod-to-core transfer, contradicting the global

207 fitting models that predict slow inter-cylinder transfer[35], but the overall flow of energy through the

208 whole PBS obtained from our model matches the experimental data well (Extended Data Fig. 7a, b).
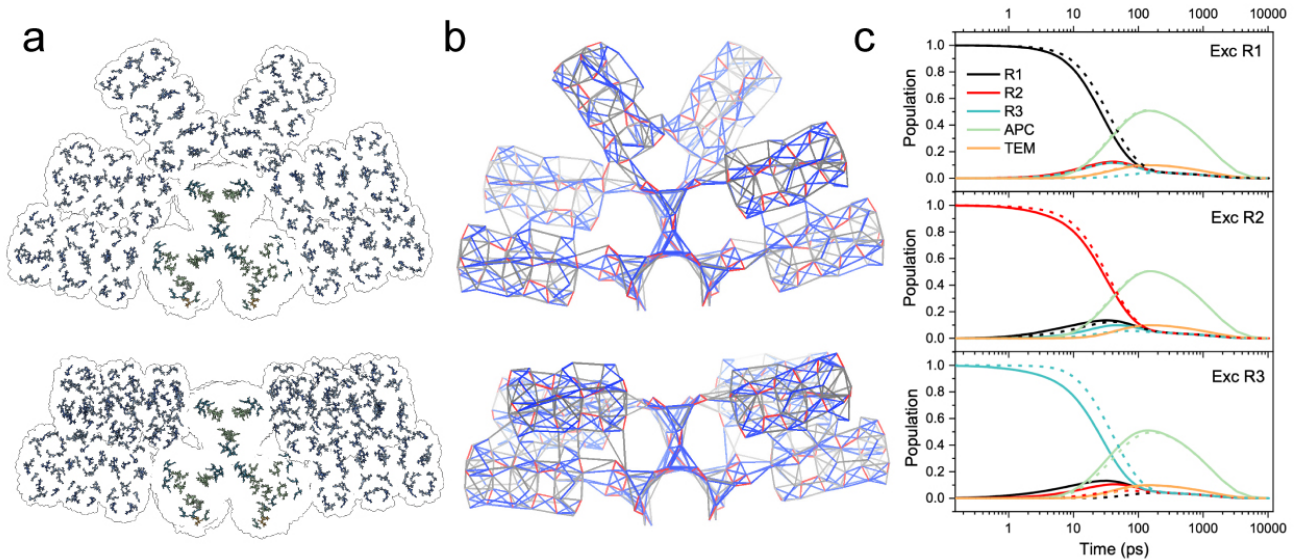
Figure 5: Energy flow through the PBS. ***a****, Pigment distribution within PBS^{up-up} (top) and PBS$^{down-down}$ (bottom).* ***b****, Maps of individual inter-pigment energy transfer rates of PBS^{up-up} (top) and PBS$^{down-down}$ (bottom). The color bars correspond to rates faster than 1 ps (red), in the 1-10 ps range (blue) and in 10-20 ps range (grey). Inter-pigment rates slower than 20 ps are omitted.* ***c****, Energy flow through down-down (solid) and up-up (dashed) PBS configurations. The excitation is placed either on the mobile rod R1 (top), middle rod R2 (middle) or bottom rod R3 (bottom). The curves monitor the evolution of excited state population of pigments located in rod, core (APC), and terminal emitters (TEM).*

The individual rate constants shown in the map are used to calculate how long the excitation resides in each structural (e.g., rod or core) or spectroscopic unit (Methods, Extended Data Fig. 7a, b). Using this approach, we also investigated the energy transfer through both the up-up and the down-down PBS conformations by placing the excitation to the most distant disc of the respective rods (Fig. 5c). For both conformations, the excitation reaches the APC core in less than 100 ps, in agreement with experimental data (see Extended Data Fig. 7a, b). Moving the mobile rod to the down position (solid lines in Fig. 5c) facilitates inter-rod energy transfer, as the more packed conformation increases the probability of energy transfer between bilins from different rods. Excitation of the mobile rod in down-down conformation leads to about 10 % population of the lowest rod, while for the up-up conformation the population of this rod is essentially zero (Fig. 5c). The same effect occurs for excitation of the bottom rod; essentially no inter-rod energy transfer is observed for the up-up conformation, while a

227 non-negligible population is found at the other rods in the down-down PBS (Fig. 5c). Thus, the more

228 compact down-down conformation allows for more pathways to reach the core, slightly increasing the

229 overall trapping efficiency. On the other hand, the fact that significant movement of the mobile rod

230 keeps the overall flow of energy through the system virtually unchanged points to robustness of PBS

231 with respect to light-harvesting capacity. The robustness of PBS is further underscored by comparison

232 with the red algal PBS, which shows that the overall dynamics are comparable[15,16,36].

233 We note that two PBS configurations differing by their fluorescence spectra have been identified by

234 single molecule spectroscopy[37]. It is thus tempting to associate the up-up and down-down

235 conformations with those two species. Here, however, the structures of up-up and down-down

236 conformations do not yet reveal any influence on the structure of the PBS core that is needed to change

237 the fluorescence of terminal emitters. Thus, the relation of the two species identified by different

238 methods remains to be defined.

239 **Importance of conformational switching for light harvesting**

240 The quality of our structural data and the various proportions of the three PBS conformations suggests

241 that we have captured previously unknown conformations of the cyanobacterial antenna. Why have

242 the different rod conformations not been described before? In retrospect, it becomes clear that during

243 earlier attempts to visualize the cyanobacterial PBS different conformation were probably confounded

244 with general flexibility[22] or likely disregarded as damaged particles[38]. Other methods to determine the

245 structural arrangement of the rods like crosslink-MS are not suited to distinguish between inter and

246 intra-rod contacts and therefore are likewise blind to the conformations we identified[29,39]. Because the

247 static rods already display two different hinge conformations, it is unlikely that the rod movement is

248 an artifact from sample preparation or imaging. The observed movement is directional and

249 quantifiable, hallmarks of true biologically relevant conformational changes. It is tempting to assume

250 that the mechanistic cause for the rod movement is coupled to the transfer of excitation energy through

251   the PBS. Pigment molecules can be found near several residues critical for rod movement (Fig. 3d,

252   Extended Fig. 6b), but further studies are now needed to explore whether any of the pigments within

253   the PBS can indeed trigger a conformational change and dictate rod position. The newly described

254   PBS architectures suggests a regulation of light harvesting at the level of supramolecular organization

255   in the thylakoid membrane that is somehow regulated by rod movement.

256   We propose two scenarios for placing our structures in that context. PBS arrays efficiently pack light

257   harvesting pigments on the surface of the thylakoid membrane and thus increase the overall photon

258   absorption cross-section of a cell. Additionally, they create redundancy of light harvesting and

259   photochemical energy conversion at the reaction centers and can thus alleviate energetic losses due to

260   damaged PSII. Using the published structure of an array as a model[40], we found that only the 'up-up'

261   state of the PBS could be fitted into the array (Extended Data Fig. 7c). Modeling of the energetics of

262   our structure in arrays indicates that lateral energy transfer between PBSs within an array is possible,

263   mainly between adjacent PBS cores.

264

265   Under certain conditions, PBS arrays might need to be dismantled to rebalance PSII versus PSI

266   excitation pressure. Given that the down-down and down-up PBS conformations cannot be fitted into

267   arrays, (Extended Data Fig. 7d, e), a conformational change in one PBS unit could therefore help to

268   break up such arrays by acting as a terminator or interrupter of PBS array formation.

269   The second scenario in which PBS conformation may regulate the balance between light harvesting

270   and photoprotection is coupled with the activity of the photoreceptor OCP. OCP quenches the

271   excitation energy by converting it to vibrational energy. Activated OCP binds to the lateral side of the

272   PBS core in the space between the rods[41]. However, the binding site is completely blocked when the

273   mobile rod is in the 'down' position. Therefore, the mobile rod controls access of OCP to the PBS core

274   and determines whether the PBS can be quenched.

275

276   Having more than one mechanism could be a means for the cell to fine tune its light harvesting

277   efficiency to adjust to altered metabolic and cellular requirements. Moreover, these scenarios are not

278   mutually exclusive and could work concurrently, but on different time scales, to adjust light-harvesting

279   in response to environmental changes. The OCP binding site is still accessible in PBS arrays[41], and

280   thus PBS arrays are readily available for OCP induced excitation energy quenching upon rapid changes

281   in the environment. Supramolecular rearrangements of the photosynthetic machinery can then take

282   place to rebalance light harvesting, which might involve rod movement and array dispersion. Several

283   studies have revealed that excitation energy harvested at the PBS can be transferred to PSI[39]. Given

284   that PSI does not require excitation energy quenching at the light-harvesting system, it can be

285   hypothesized that the down-down position obscuring the OCP binding site might be involved mainly

286   in transferring its harvested energy to PSI. In fact, in such a scenario, OCP induced quenching would

287   be counterproductive.

288

289   Here, we present the first high-resolution structures of cyanobacterial phycobilisomes, revealing an

290   unexpected variety of conformational states that help to collect and deliver light energy to

291   photosynthetic reaction centers. Further analysis of these structures will inform future experiments that

292   will help us to understand and harness the power of these large light harvesting machines.

293

294

295

296

297

298

299

300

Methods

Preparation of the *Synechocystis* PCC 6803 Phycobilisome

Synechocystis PCC 6803 were grown photoautotrophically in a BG11 medium. Cells were kept in a rotary shaker (100 rpm) at 30°C, under 3% CO_2 enrichment, illuminated by white fluorescent lamps with a total intensity of about 30 µmol photons m^{-2} s^{-1}. The protocol used for PBS isolation was based on[42,43]. The cells were collected at 8,000 rpm, 10 min at room temperature. The pellet was resuspended in 10 mL of PBS isolation buffer (0.75 M potassium phosphate buffer pH 7.5, 1 mM EDTA, 0.5 mM PMSF) per 2 g of fresh weight of cells. Then, the cells were washed twice by centrifugation at 30,000 *g* during 15 min. The cells were broken through French Press at 1,000 psi three times. The supernatant was incubated in the presence of 2% (v/v) Triton X-100 under dim stirring, at 23°C, 15-20 min. The cell debris and the aggregates were removed by ultracentrifugation at 20,000 rpm (Ti-70 rotor) for 20 min at room temperature. The dark blue supernatant was directly loaded onto a discontinuous sucrose gradient (0.5, 0.75, 1, and 1.5 M sucrose layers in 0.75 M potassium phosphate buffer, pH 7.5), and spun at 150,000 *g*, 23°C, for 16 h using a SW28 rotor. The intact PBS was recovered from the 0.75 – 1 M interface of the sucrose gradient. The PBS were buffer exchanged into 0.75 M potassium phosphate buffer pH 7.5 using Amicon (30 kDa). The samples were kept at room temperature for further use.

Protein separation

The isolated PBS samples were concentrated by precipitation with 20% (v/v) trichloroacetic acid prior to loading on a sodium dodecyl sulfate-polyacrylamide gel electrophoresis (SDS-PAGE) 5-20% gradient gel. The gels were run for 25 min at 240 V and were stained by Coomassie Brilliant Blue. The protein composition of the SDS-PAGE confirms the presence of all PBS subunits (Extended Data Tables 1, 2).

324 **Absorption and fluorescence spectrum measurement**

325 PBS ultraviolet–visible (UV-vis) absorption spectra were collected with a Cary 60 spectrophotometer

326 (Agilent). The fluorescence emission spectra of the PBS were recorded at room temperature from 600

327 to 800 nm in a fluorimeter (TECAN Spark 20M multimode microplate reader) with an excitation

328 wavelength of 580 nm.

329 **PBS biotinylation**

330 The   ChromaLink™   Biotin   Labeling   reagent,   purchased   from   Solulink   (see

331 https://vectorlabs.com/chromalink-biotin-antibody-labeling-kit.html), was used as it incorporates a

332 chromophore as part of the linker. 120 μl of the PBS in 0.75 M potassium-phosphate pH 7.5 was buffer

333 exchanged with the 1X Modification buffer (10X Modification buffer- 100 mM sodium phosphate and

334 150 mM sodium chloride pH 8.0-diluted in 0.75 M potassium-phosphate pH 8.0). Then, the sample

335 amount was quantified using an absorbance spectrum and using the values at 280, 354 and 620 nm to

336 calculate the amount of biotin to add to the reaction. The samples were then incubated for 120 min at

337 room temperature. The sample was buffer exchanged back into 100 μl of 0.75 M potassium-phosphate

338 pH 7.5 using a Zeba Spin Desalt 7 kDa MWCO column, Thermo Scientific). UV–vis spectra were

339 measured from 230–800 nm for biotinylated protein samples using a Tecan Safire microplate reader.

340 Using the absorbance values at 280, 354 and 620 nm, and the molar extinction coefficients, the average

341 number of biotin molecules covalently attached per PBS were calculated to be about 1. Fluorescence

342 emission spectra were used to confirm functional energy transfer in the isolated PBS before and after

343 biotinylation (Extended Data Fig. 1d).

344 **Cryo-EM sample preparation from purified PBS**

345 For sample preparation we used Quantifoil Au 300 mesh 2/1 grids covered with a home-made

346 streptavidin monolayer, which were manufactured as described previously[30]. To apply the sample,

347 grids were first rehydrated in buffer A (375 mM potassium phosphate, pH 7.5) and then blotted dry

348 with filter paper. 4 μl of PBS sample at 5.3 mg/ml in buffer B (750 mM potassium phosphate, pH 7.5)

349 were added to the grid and then incubated on the bench for 60 seconds. Grids were washed on two 10

350 μl drops of buffer C (375 mM potassium phosphate, pH 7.5, 3% w/v trehalose, 0.01% v/v NP40, 0.05%

351 w/v beta-octylglucoside) before being carefully wicked with Whatman filter paper. 1 μl of buffer C

352 was added quickly, and the grid lifted into a FEI Mark IV Vitrobot. The grid was then manually blotted

353 for 2-3s at 18°C and 100% humidity before plunging into a liquid ethane-propane (3:1) mix[44]. During

354 the process, the PBS was exposed to ambient light for a total of approximately 2-3 min between

355 pipetting and vitrification.

356 **Cryo-EM data collection PBS**

357 For initial assessment of the sample, grids were loaded onto a Talos Arctica microscope (Thermo

358 Fisher Scientific) equipped with a Gatan K3 direct electron detector and operating at 200 kV. 1954

359 movies were collected at a super-resolution pixel size of 0.558 Å, a defocus range of -0.6 μm to -1.8

360 μm and a total exposure of 50 e⁻/Å² using SerialEM[45]. Images were processed as described below.

361 After evaluation of the first dataset, a second dataset was collected on a Titan Krios G3i microscope

362 operating at an accceleration voltage of 300 kV, equipped with a Gatan K3 direct electron detector

363 operating in CDS mode[46] and a GIF Quantum energy filter with a 20-eV slit width. 12,051 movies

364 were acquired with SerialEM in super-resolution counting mode with a super-resolution pixel size of

365 0.525 Å using an image shift collection scheme with active beam tilt correction, a defocus range from

366 -0.5 μm to -1.6 μm and a total electron exposure of 50 e⁻/Å².

367 **Image processing**

368   All movies were aligned, gain corrected and binned by 2 using MotionCorr2 as implemented in

369   RELION3[47]. The background streptavidin lattice in the motion corrected micrographs was subtracted

370   using in-house scripts[30]. These subtracted micrographs were then imported into Cryosparc[48] for patch

371   CTF estimation and further image processing. For dataset 1 from the Talos Arctica microscope,

372   particles were picked using the blob picker, extracted with a box size of 720 pixels, and subjected to

373   one round of 2D classification. Good classes representing different views of the PBS were selected

374   and used as templates for a second round of autopicking, yielding ~156,000 particles. After another

375   round of 2D classification, ~43,000 particles in good classes were used to generate an ab-initio model

376   of the PBS. A subsequent round of heterogenous refinement using this reference yielded two distinct

377   classes representing the $PBS^{up\text{-}down}$ (66 %) and $PBS^{up\text{-}up}$ (34 %) conformations. These classes were

378   refined to 4.1 Å and 4.5 Å, respectively.

379   For dataset 2 from the Titan Krios microscope, particles were picked from 800 micrographs using

380   templates generated from the $PBS^{up\text{-}up}$ reconstructions from dataset 1. After 2D classification and

381   heterogenous refinement three distinct classes corresponding to $PBS^{up\text{-}down}$, $PBS^{up\text{-}up}$ and $PBS^{down\text{-}down}$

382   conformations became apparent. Using these classes as references, 11,903 micrographs were picked

383   to yield ~1,900,000 particles. After several rounds of heterogenous refinement, approximately 510,000

384   good particles were sorted into four classes representing the three conformations ($PBS^{up\text{-}down}$ 50.6%,

385    $PBS^{up\text{-}up}$ 38.9%, and $PBS^{down\text{-}down}$ 10.5%). Refinement of the three conformations yielded overall

386   resolutions of 2.7 Å ($PBS^{up\text{-}up}$), 2.8 Å ($PBS^{up\text{-}down}$) and 3.5 Å ($PBS^{down\text{-}down}$).

387   During initial rounds of 2D classification of the datasets, we observed that several classes

388   corresponded to PBS-rods that aligned independently of the core section of the PBS. To obtain

389   reconstructions of the rods, these classes were used as templates for autopicking on a subset of 500

390   micrographs of dataset 2 and extracted with a box size of 360 pixels. 2D classification followed by ab-

391   initio model generation and heterogenous refinement yielded a particle set that reached a resolution of

392   2.9 Å during non-uniform refinement. Using the same templates for picking from the entire dataset 2,

393   ~2,100,000 good particles were obtained that refined to a resolution 2.1 Å after CTF refinement,

394   reaching Nyquist frequency. Further classification of the particle set to distinguish between different

395   rod protomers within one PBS complex was unsuccessful and always yielding the same conformation.

396   To visualize the contact area between two neighboring rods in the PBS$^{up\text{-}down}$ conformation, particle

397   subtraction followed by local refinement was carried out on the PBS$^{up\text{-}down}$ reconstruction. The map

398   yielded an improved resolution of 2.6 Å.

399   All processing was carried out using C1 symmetry and resolutions were estimated with the FSC =

400   0.143 criterion[49]. Reconstructions were sharpened using DeepEMhancer[50] with the default tight mask

401   preset.

402   **Atomic model building and refinement**

403   Using our PBS-OCP^R atomic models as a basis[41], atomic models of the PBS core were refined using

404   a cropped PBS$^{up\text{-}down}$ map with the real space refinement program in PHENIX 1.19.2 (ref. [51]). Similarly,

405   models of the core of other PBS conformations were refined but found to be virtually identical. Models

406   of the PBS-OCP^R rod were used as a basis for refinement of the PBS rod. To arrive at models for all

407   three holo-PBS complexes, maps and models for the individual rods were rigid-body docked into the

408   density of each holo-PBS conformer, which resulted in an unambiguous orientation of each rod.

409   Because the holo-PBS maps are not resolved enough in the distal rod regions to allow for model

410   refinement, models of the full complexes are for visualization only.

411   **LC-MS/MS analysis of the PBS SDS-PAGE fractions**

412   Gel bands were digested in-gel according to[52] with modifications. Briefly, gel bands were dehydrated

413   using 100 % acetonitrile and incubated with 10 mM dithiothreitol in 100 mM ammonium bicarbonate,

414   pH~8, at 56 ºC for 45 min, dehydrated again and incubated in the dark with 50 mM iodoacetamide in

415   100 mM ammonium bicarbonate for 20 min. Gel bands were then washed with ammonium bicarbonate

416 and dehydrated again. Sequencing grade modified trypsin was prepared to 0.01 μg/μl in 50 mM

417 ammonium bicarbonate and ~100 μl of this was added to each gel band so that the gel was completely

418 submerged. Bands were then incubated at 37 ºC overnight. Peptides were extracted from the gel by

419 water bath sonication in a solution of 60% Acetonitrile (ACN) /1% Trifluoroacetic acid (TFA) and

420 vacuum dried to ~2 μl.

421 Dried samples were re-suspended to 20 μl in 2% ACN/0.1% TFA and an injection of 5 μl was

422 automatically made using a Thermo (www.thermo.com) EASYnLC 1000 onto a Thermo Acclaim

423 PepMap RSLC 0.1mmx20mm C18 trapping column and washed for ~5 min with buffer A. Bound

424 peptides were then eluted over 35 min onto a Thermo Acclaim PepMap RSLC 0.075mm x 250mm

425 resolving column with a gradient of 5%B to 40%B in 24 min, ramping to 90%B at 25 min and held at

426 90%B for the duration of the run (Buffer A = 99.9% water/0.1% formic acid, Buffer B = 80%

427 acetonitrile/0.1% formic acid/19.9% water) at a constant flow rate of 300 nl/min. Column temperature

428 was maintained at a constant temperature of 50 °C using and integrated column oven (PRSO-V1,

429 Sonation GmbH, Biberach, Germany).

430 Eluted peptides were sprayed into a ThermoScientific Q-Exactive mass spectrometer

431 (www.thermo.com) using a FlexSpray spray ion source. Survey scans were taken in the Orbitrap

432 (70,000 resolution, determined at m/z 200) and the top 15 ions in each survey scan are then subjected

433 to automatic higher energy collision induced dissociation (HCD) with fragment spectra acquired at

434 17,500 resolution. The resulting MS/MS spectra are converted to peak lists using Mascot Distiller,

435 v2.7.1 (www.matrixscience.com), and searched against a database containing all *Synechocystis* PCC

436 6803 protein sequences and appended with common laboratory contaminants (downloaded 2020-11-

437 17 from www.uniprot.org and www.thegpm.org, respectively) using the Mascot searching algorithm,

438 v2.7. The Mascot output was then analyzed using Scaffold, v5.0 (www.proteomesoftware.com) to

439 probabilistically validate protein identifications. Assignments validated using the Scaffold 1%FDR

440 confidence filter are considered true.

441   Thee performed LC-MS/MS on the protein bands to confirm the identity of all the PBS components

442   (Extended Data Table 2).

443   **Modelling the energy flow within PBS complex.**

444   Excitation energy transfer within PBS was studied in the limit of the Förster theory, using dipole-

445   dipole approximation for the inter-pigment coupling. The energy transfer rates k (in ps^{-1}) were

446   computed using the equation[53]:

$$k_{ij} = 1.18 \, V^2 J \tag{1}$$

448   where J is the spectral overlap between donor emission and acceptor absorption, and the coupling V

449   (in cm^{-1}) is given by

$$V = 5.04 \frac{\mu_i \mu_j \kappa}{R^3} \tag{2}$$

451   where R is the center-to-center dipole separation in nm, k is the orientation factor, and μ_i and μ_j are the

452   transition dipole moments (in Debye) of the donor and acceptor, respectively. We have used effective

453   transition dipole moments, including the correction for the effect of dielectric properties of the protein

454   (see ref.[53] for discussion of this point). The direction of the pigment transition dipoles of bilin

455   chromophores were placed along the axis of the conjugated parts of the molecules. The geometrical

456   axis was obtained using the singular-value decomposition on the atom coordinates. For bilins, the

457   transition dipole moment of 13 D were used for the bilins in rod (CPC), and 15 D for bilins in the core

458   (APC) pigments[54]. The spectral overlap J is calculated from the area-normalized spectra of donor and

459   acceptor reported in literature[34,55,56]. Using the full matrix of the excitation transfer rates computed

460   using (1), it is possible to write down a master equation describing the time evolution of probability of

461   exciton residence on i-th chromophore, with a vector-valued $y(t) = y_i$(t) (for i running from 1 to the

462   number of pigments):

$$\frac{d\boldsymbol{y}(t)}{dt} = \boldsymbol{K} \cdot \boldsymbol{y}(t) \tag{3}$$

464

23

465 where $\boldsymbol{K}$ represents the transition matrix whose off-diagonal elements (K_{ij}) represent the pairwise rates

466 of energy transfer, k_{ij}, between donor (i) and acceptor (j) pigments. The diagonal elements are defined

467 as:

468
$$K_{ii} = -\left(k_{ii}^0 + \sum_{i,i \neq j} k_{ij} \right) \tag{4}$$

469

470 where k_{ii}^0 corresponds to the intrinsic excited state decay rate of the i-th pigment; we used $k_{ii}^0 = (1500$

471 ps$)^{-1}$ for all bilins, except for b-84, which was assigned the lifetime of 900 ps, based on[57], however,

472 the exact value of this parameter has little effect on the simulation results. Solving (3) for initial

473 conditions given as $y_i(0) = 1$ for $i = k$, and $y_i(0) = 0$ for $i \neq k$, yields the model for the excitation

474 flow through the PBS following excitation into k-th pigment. A sum of $y_i(t)$ over i then describes the

475 total decay of the excitation in the PBS. The validity of the model was tested by comparing the results

476 with experimental data reported earlier. Extended Data Fig. 7 shows that correspondence between the

477 simulation and experimental data is reasonable, considering that the model was not in any way adjusted

478 to fit the experimental data and is based solely on the structural information and previously reported

479 pigment spectra.

480 **Bioinformatics**

481 Homologues of ApcG were found by searching with a profile HMM (constructed from sll1873

482 homologs obtained by BLAST search) against 420 non-redundant UniProt proteomes that contained a

483 complete PBS protein set (as described in ref.[41]). Sequences of the 50 proteomes with a protein

484 composition closest to *Synechocystis* PCC 6803 were used for sequence alignments. Sequences were

485 aligned ClustalW[58,59], trimmed with trimAl[60] and the protein sequence conservation was visualized

486 with Weblogo 3.74[61].Homologues of ApcG were found by searching with a profile HMM (constructed

487 from sll1873 homologs obtained by BLAST search) against 420 non-redundant UniProt proteomes

488   that contained a complete PBS protein set (as described in ref.[41]). Sequences of the 50 proteomes with

489   a protein composition closest to *Synechocystis* PCC 6803 were used for sequence alignments.

490   Sequences were aligned ClustalW[58,59], trimmed with trimAl[60] and the protein sequence conservation

491   was visualized with Weblogo 3.74[61].

492   Structures were analyzed with ChimeraX[62] and Pymol (The PyMOL Molecular Graphics System,

493   version 1.7 Schrödinger, LLC).

Acknowledgements

Author contributions

508   MADM and PVS designed and performed experiments, interpreted results. CK designed and

509   supervised the project. HK helped with the sample preparation, interpreted results. MS refined the

510   structures and interpreted results. DB and TP performed the model for the energy transfer. BJG

511 performed initial characterization of the specimen for cryo-EM. MADM, PVS and CK wrote the

512 manuscript with help from all authors.

513 **Competing interest**

514 The authors declare no competing interests.

515 **Data availability**

516 The atomic coordinates have been deposited in the Protein Data Bank with the accession codes 7SC8

517 for the rod and 7SC7 for the PBS$^{\text{up-down}}$ core.

518 The EM maps have been deposited in the Electron Microscopy Data Bank with the accession codes

519 25029 for the rod, 25028 for the PBS$^{\text{up-down}}$ core, 25069 for the full map of the PBS$^{\text{up-down}}$ conformation

520 and the rod-rod contact, 25070 for the full map of the PBS$^{\text{down-down}}$ conformation and 25071 for the

521 full map of the PBS$^{\text{up-up}}$ conformation.

522 All other data are available from the corresponding authors upon reasonable request.

523 **Extended Data**

524 ***Extended Data Table 1: Synechocystis PCC 6803 Phycobilisome Protein subunits.*** *(*) Nomenclature used along the text.*

525 *(**) New linker discovered and incorporated in this study.*

Protein component	Gene symbol	Protein name (*)	Function	pfam	#bilins per monomer	#proteins per PBS	MW (kDa)
α-PC	*cpcA*	CpcA	Rod antenna protein	pfam00502	1 PCB	108	17.6
β-PC	*cpcB*	CpcB	Rod antenna protein	pfam00502	2 PCB	108	18.1
L$_{R33}$	*cpcC1*	CpcC1	Internal rod linker	pfam00427/ pfam01383	--	6	32.5
L$_{R30}$	*cpcC2*	CpcC2	Internal rod linker	pfam00427/ pfam01383	--	6	30.8
L$_{R10}$	*cpcD*	CpcD	Internal rod linker	pfam01383	--	6	9.3
L$_{RC}$	*cpcG1*	CpcG1	Rod-to-core linker	pfam00427	--	6	28.9
L$_{RC}$	*cpcG2*	CpcG2	Rod-to-core linker	pfam00427	--	--	28.5
α-APC	*apcA*	ApcA	Major core antenna protein	pfam00502	1 PCB	32	17.4
β-APC	*apcB*	ApcB	Major core antenna protein	pfam00502	1 PCB	34	17.2

Structures of the Cyanobacterial Phycobilisome

L_C	*apcC*	ApcC	Internal core protein	pfam01383	--	6	7.7
L_{CM}	*apcE*	ApcE	Core-to-membrane linker	pfam00427/ pfam00502	1 PCB	2	100.3
α-B	*apcD*	ApcD	Minor core antenna protein	pfam00502	1 PCB	2	17.9
α-B18	*apcF*	ApcF	Minor core antenna protein	pfam00502	1 PCB	2	18.9
L_{C10}[**]	*apcG*	ApcG	Linker	Newly discovered no assigned pfam	--	2	12.9

526

527   ***Extended Data Table 2: MS analysis of the Synechocystis PCC 6803 Phycobilisome Protein subunits.*** *The criteria were*

528   *2 peptides, False Discovery Rate (FDR) = 1%, percentage of coverage (% coverage) > 30%, and the number of total*

529   *peptide count of each protein (# total peptide count). MW (kDa) = Molecular Weight assigned by the software used in the*

530   *analysis, Scaffold 5.0 software.*

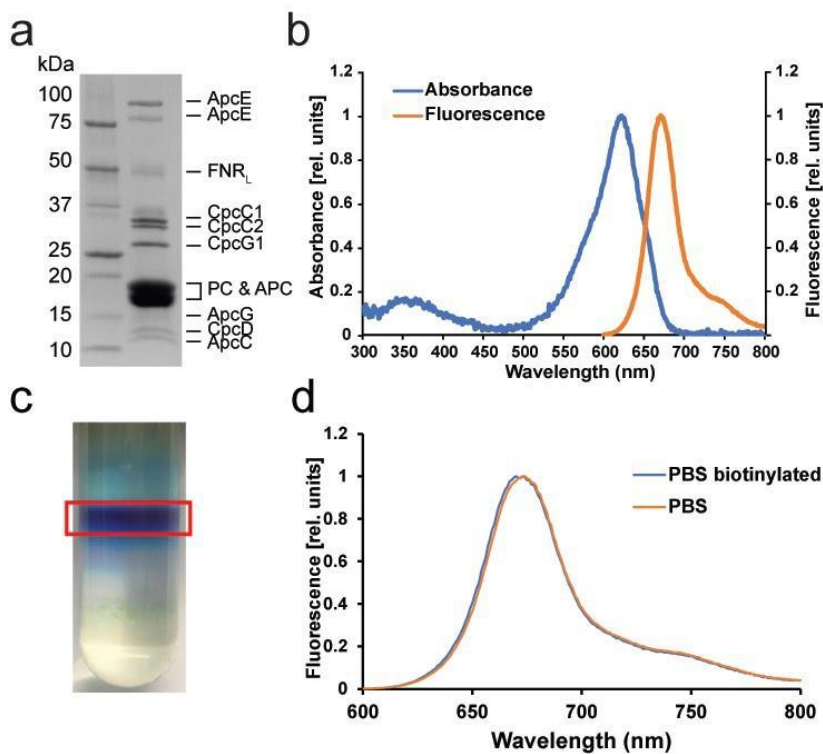| Protein component	Gene symbol	# total peptide count	% coverage	MW (kDa)
α-PC	*cpcA*	420	94	18
β-PC	*cpcB*	414	93	18
L_{R33}	*cpcC1*	236	61	33
L_{R30}	*cpcC2*	219	60	31
L_{R10}	*cpcD*	148	88	9
L_{RC}	*cpcG1*	215	83	27
L_{RC}	*cpcG2*	21	43	29
α-APC	*apcA*	224	93	17
β-APC	*apcB*	322	94	17
L_C	*apcC*	86	63	8
L_{CM}	*apcE*	671	72	100
α-B	*apcD*	61	83	18
α-B18	*apcF*	66	71	19
L_{c10}	*apcG*	27	78	13
FNR	*petH*	177	78	46
α-PC	*cpcA*	420	94	18
β-PC	*cpcB*	414	93	18
L_{R33}	*cpcC1*	236	61	33
L_{R30}	*cpcC2*	219	60	31
L_{R10}	*cpcD*	148	88	9
L_{RC}	*cpcG1*	215	83	27
L_{RC}	*cpcG2*	21	43	29
FNR	*petH*	177	78	46

29

Structures of the Cyanobacterial Phycobilisome

531 ***Extended Data Table 3: Cryo-EM data collection, refinement and validation statistics***

	PBS$^{up\text{-}up}$	PBS$^{up\text{-}down}$	PBS$^{up\text{-}up}$ 25071	PBS$^{up\text{-}down}$ 25069	PBS$^{up\text{-}down}$ core 25028 7SC7	PBS$^{down\text{-}down}$ 25070	Rod 25029 7SC8
EMD							
PDB							
Dataset	1		2				
Data collection and processing							
Magnification	36000 x		81000 x				
Voltage (kV)	200		300				
Electron exposure (e–/Å^2)	50		50				
Defocus range (μm)	0.6-1.8		0.5-1.6				
Pixel size (Å)	1.115		1.05				
Symmetry imposed	C1		C1				
Initial particle images (no.)	156,000		1,9M				6.6M
Final particle images (no.)	14,434	28,109	135,701	202,719		52,674	2.1M
Map resolution (Å)	4.5	4.2	2.7	2.8		3.5	2.1
FSC threshold 0.143	(C2 imposed)						
Map resolution range (Å)	N/A	N/A	2.5-10	2.6-10		3.2-10	2.1-2.5
Refinement	N/A	N/A					
Initial model used (PDB code)					7SC9		7SCA
Model resolution (Å)					3		2.2
FSC threshold 0.5							
Model composition							
Non-hydrogen atoms					107930		54106
Protein residues					13756		6835
Ligands					72		54
B factors (Å^2)							
Protein					130.4		88.8
Ligand					125.5		88.6
R.m.s. deviations							
Bond lengths (Å)					0.003 (0)		0.002 (0)
Bond angles (°)					0.610 (207)		0.793 (13)
Validation							
MolProbity score					1.79		1.53
Clashscore					15.2		10.2
Poor rotamers (%)					0.01		0.00
Ramachandran plot							
Favored (%)					97.48		98.9
Allowed (%)					2.50		1.1
Disallowed (%)					0.01		0.00

532

30

Extended Data Figure 1: Biochemical and spectroscopic PBS characterization. a, *Protein composition analysis of the PBS sample by SDS-PAGE. Identification of the components by MS can be found in Extended Data Table 2.* ***b****, Absorption, and fluorescence spectrum of the isolated PBS in 0.75 M K-phosphate pH 7.5. The PBS shows a maximum absorbance at 620 nm corresponding to phycocyanin (PC), and a shoulder at 650 nm corresponding to allophycocyanin (APC). The fluorescence peak maximum is ~670 nm when PC is preferentially excited (excitation at 580 nm), and a shoulder from 740 nm to 780 nm.* ***c****, Sucrose gradient of PBS showing the intense blue band that was used for cryo-EM.* ***d****, Fluorescence spectra of PBS before and after in vitro biotinylation. Collectively, these data show that the PBS preparation was structurally and functionally intact.*

542
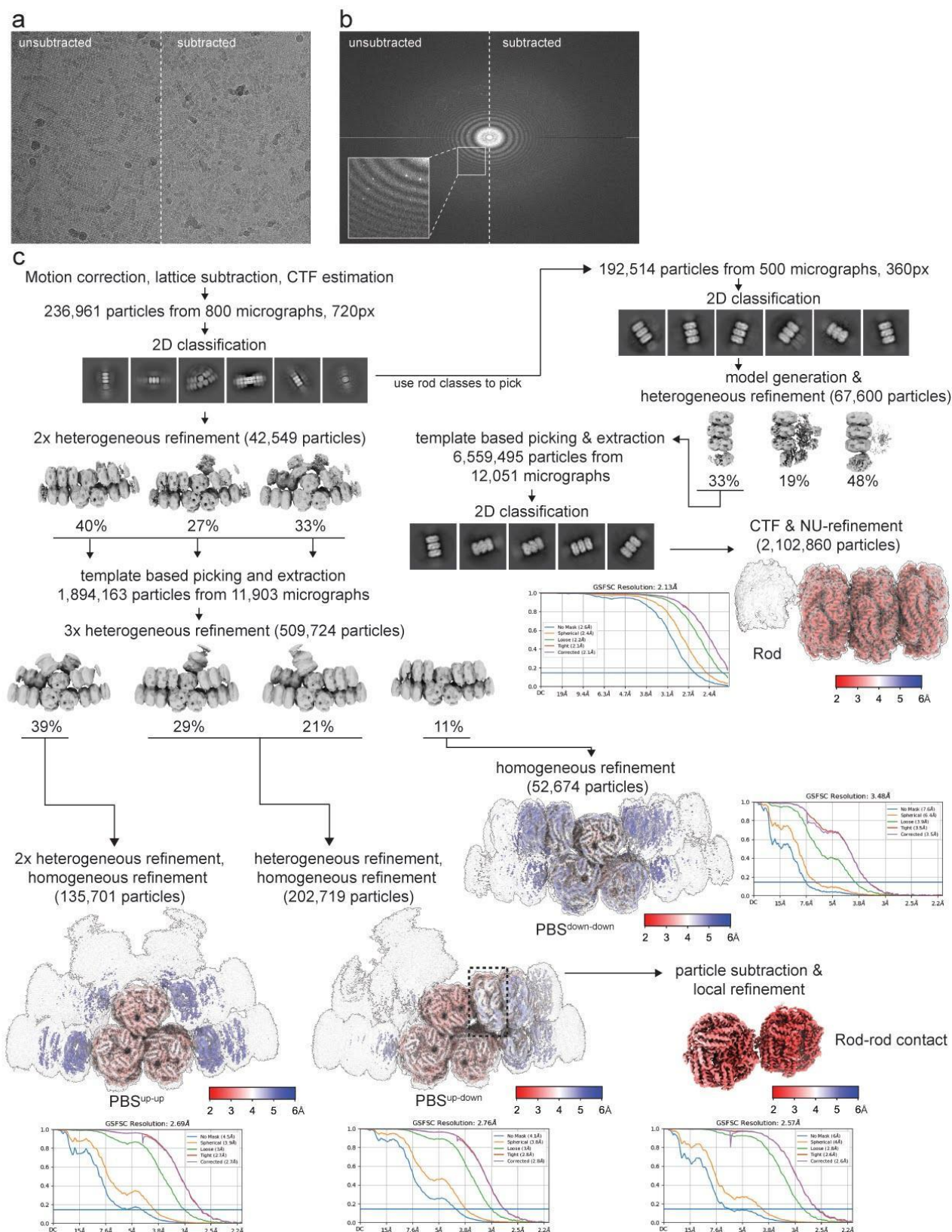
Extended Data Figure 2: Cryo-EM data processing of PBS data. *a, Example raw micrograph before and after*

*streptavidin lattice subtraction. **b**, Fourier transform of **a** showing Bragg diffraction of streptavidin crystal before*

*subtraction. **c**, Processing pipeline of dataset 2, yielding the structures presented in this paper. Red to blue color shadings*

Structures of the Cyanobacterial Phycobilisome

546   *represent local resolution estimates at FSC=0.5 ranging from 2 to 6 Å. The three PBS conformations and the structure of*

547   *the rod are shown at two different thresholds to visualize both overall shape and higher resolution details.*

Structures of the Cyanobacterial Phycobilisome
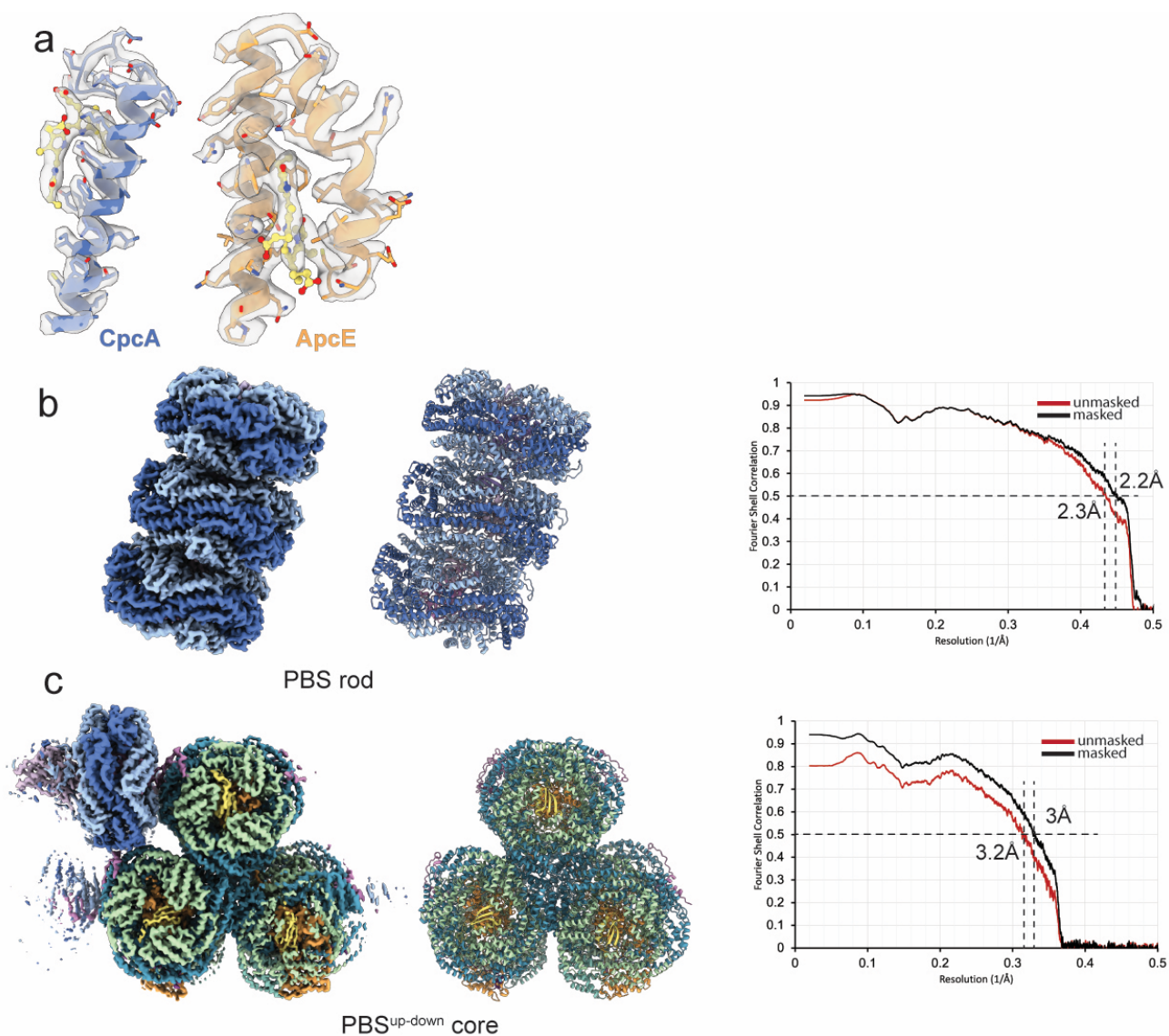
548

549 ***Extended Data Figure 3: Map and Model quality of PBS^up-down***. ***a***, *EM density examples of CpcA, ApcE and associated*
550 *bilins showing map quality of the PBS^up-down*. ***b*** *and* ***c***, *Cropped PBS^up-down map, model and corresponding Fourier shell*
551 *correlation (FSC) curves. Resolution of masked and unmasked models are indicated at FSC = 0.5.*

Structures of the Cyanobacterial Phycobilisome
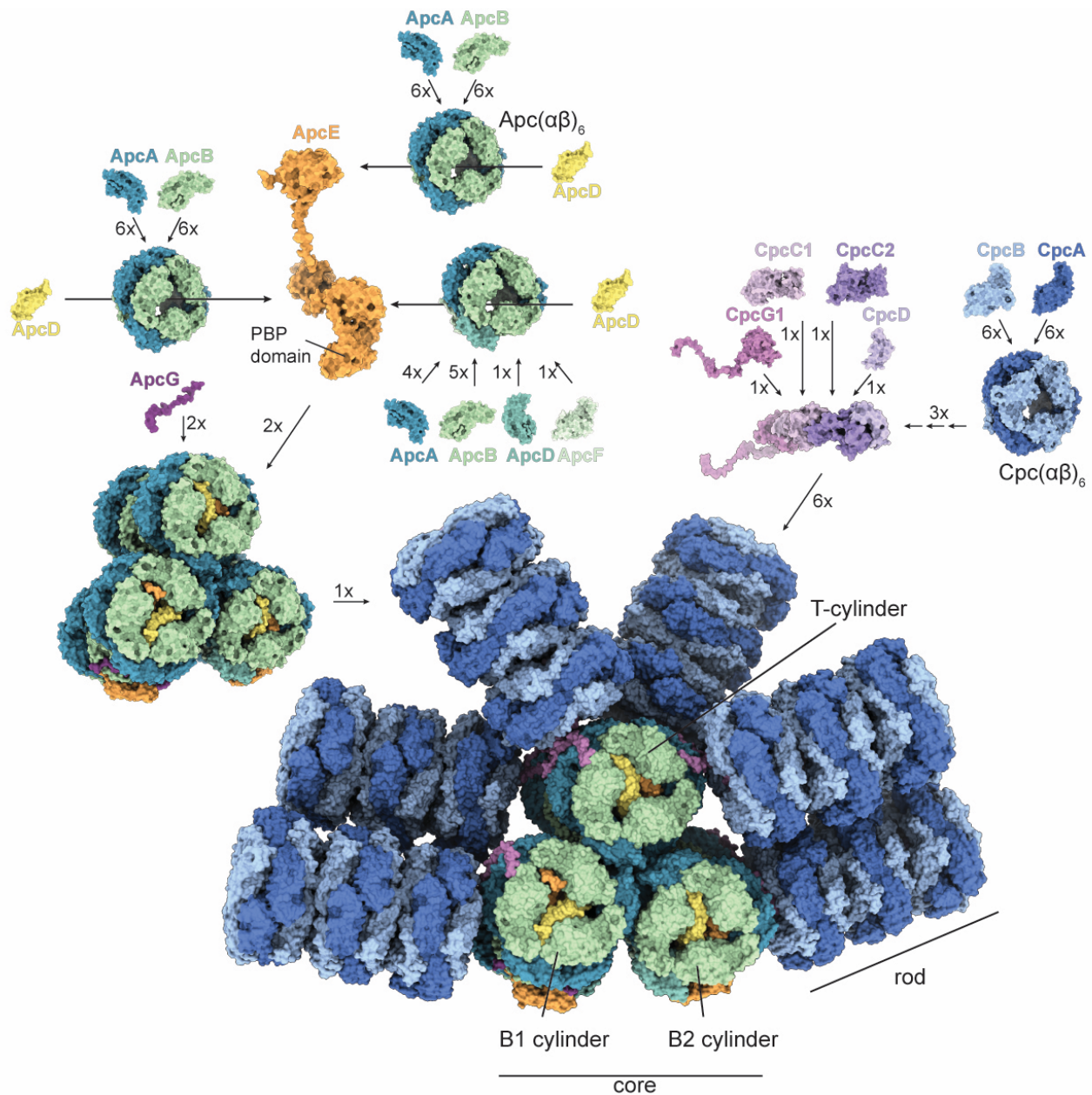
552

553 ***Extended Data Figure 4: Assembly of the PBS****. The core cylinders consist of four stacked discs; each disc contains three*

554 *α- and three β-type Apc proteins that form the signature (αβ)$_6$ hexamers. Besides the canonical ApcA and ApcB proteins,*

555 *B1 and B2 cylinders contain one copy each of ApcD and ApcF, as well as the phycobiliprotein domain of ApcE. These are*

556 *symmetrically arranged in the two bottom cylinders, oriented towards the membrane. ApcG. ApcD and ApcE protrude out*

557 *of the core, indicating their likely role in contacting the photosystems. Each rod contains three stacked discs, each*

558 *consisting of one CpcA/B hexamer. The overall architecture of the PBS core is in agreement with modelling predictions[29].*

Structures of the Cyanobacterial Phycobilisome

559
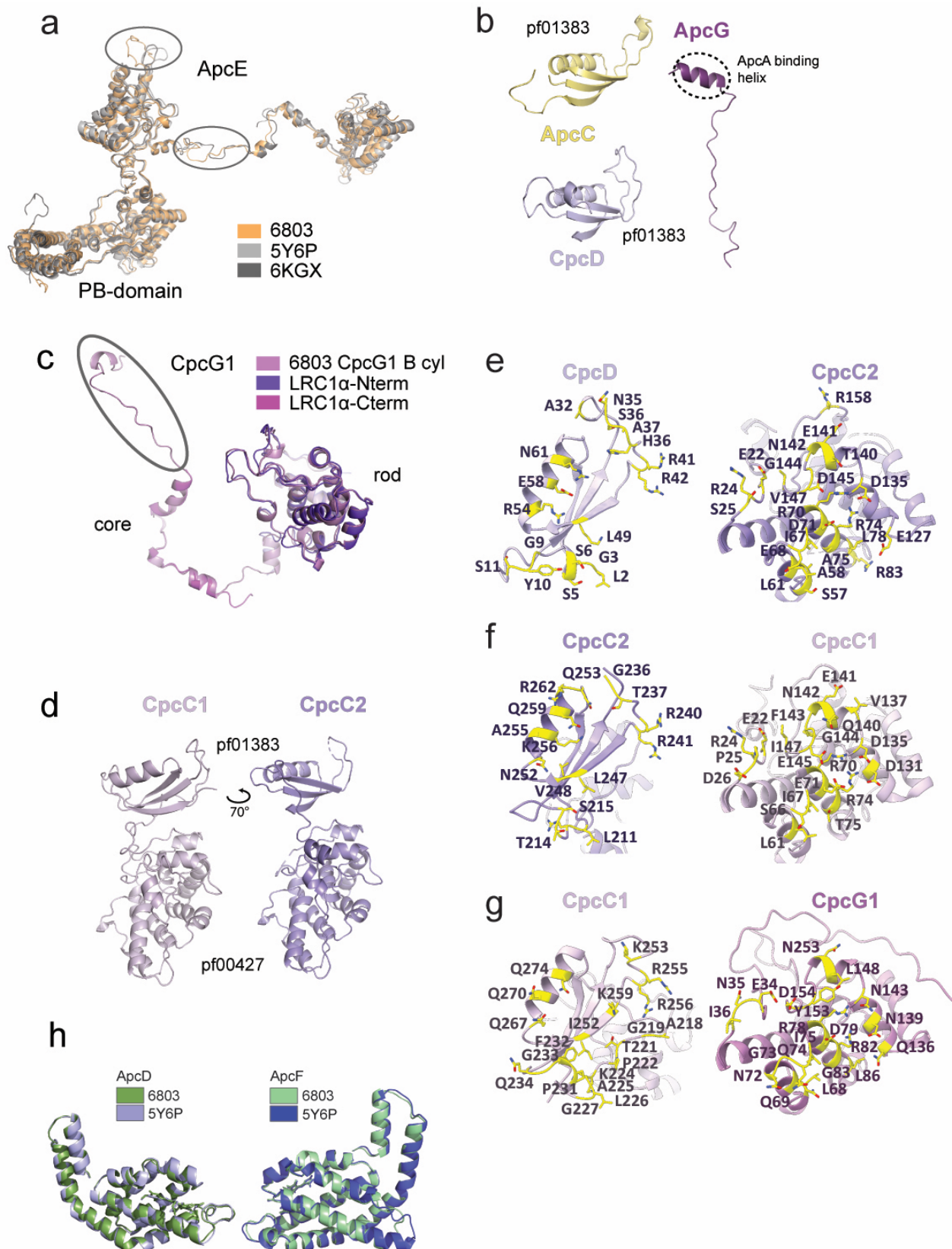
Extended Data Figure 5: Molecular details of the PBS. *a, Alignment of ApcE with red algae homologs (PDB:5Y6P*

*Griffithsia pacifica, PDB:6KGX Porphyridium purpureum). RMSD is 1.9 Å, differences are circled. b, Structural models*

of ApcC, ApcG and CpcD. CpcD and ApcC consist of a single pf01383 domain. c, Alignment of CpcG1 with red algae

563   *homologs. Circle in CpcG1 shows C-terminal domain. CpcG1 is related to algal LRC1 linker with RMSD of 0.7 Å in the*

564   *pf00427 domain. The C-terminal domain of CpcG1 has homology to LRC1a with RMSD of 0.6 Å.* ***d****, Comparison of CpcC1*

565   *and CpcC2.* ***e-g****, interaction between CpcD, CpcC2, CpcC1 and CpcG1. Interacting residues are highlighted.* ***h****, Alignment*

566   *of ApcD and ApcF with red algae homologs. ApcD is related to the red algal homolog with RMSD of 0.6 Å while ApcF*

567   *aligns with an RMSD of 0.6 Å with its homolog. The only major differences exist in loop regions.*

568

Structures of the Cyanobacterial Phycobilisome
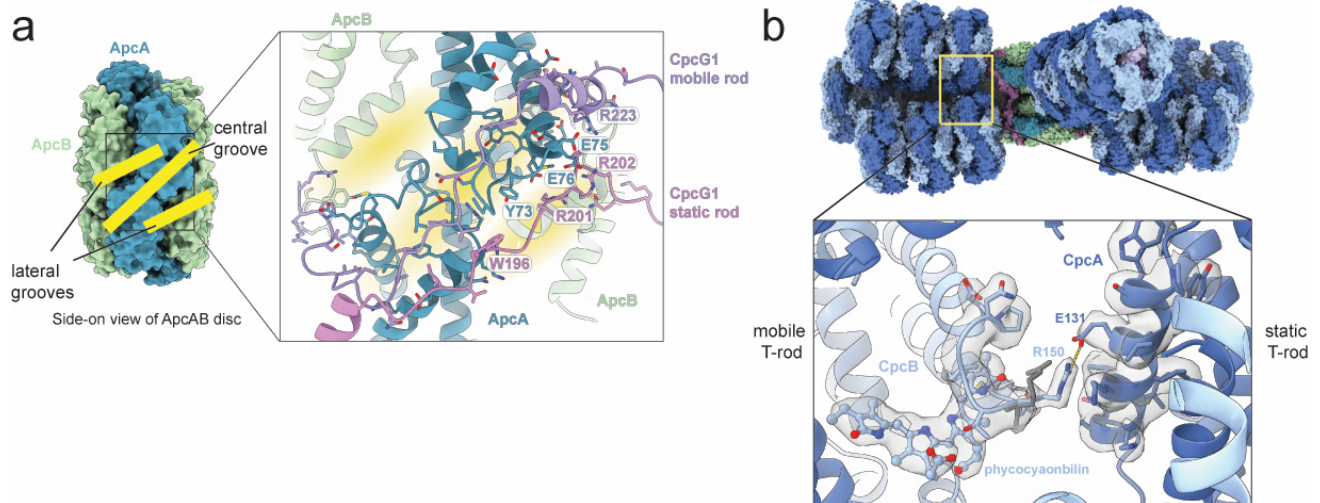
569

570 ***Extended Data Figure 6: PBS rod conformation. a**, Side view of AcpAB disc showing the groove network that organizes*

571 *CpcG1 linker attachment to the PBS core. Selected residues are labeled. **b**, Salt bridge formed between two neighboring*

572 *rods when the mobile rod adopts the 'down' conformation. EM density is transparent, dark grey and shows the*

573 *conformation of R150 when the mobile rod is 'up'. A bilin molecule in very close proximity of R150 of CpcB is also shown.*

Structures of the Cyanobacterial Phycobilisome

574
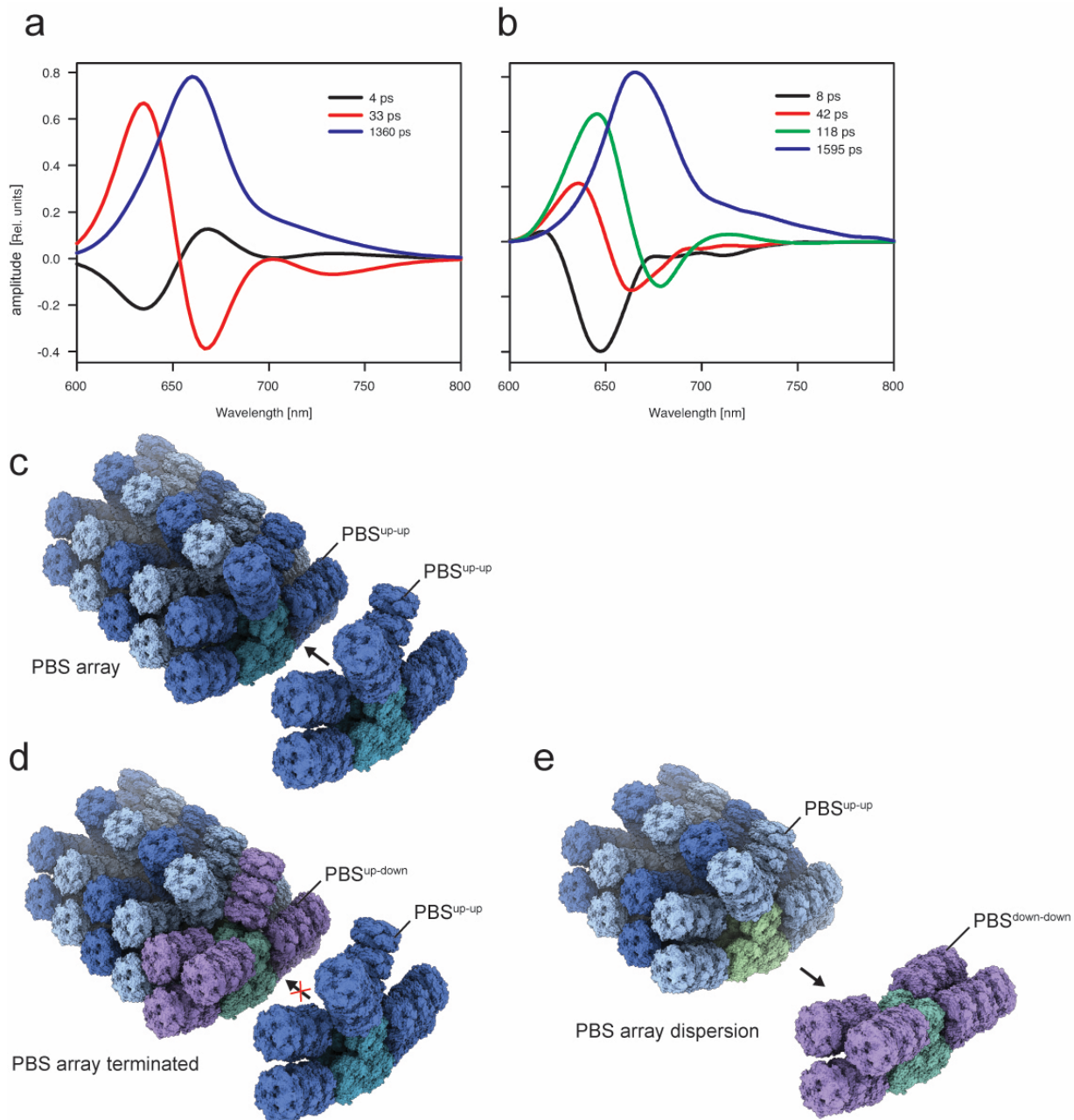
Extended Data Figure 7: Decay associated spectra (DAS) and PBS arrays. *DAS spectra obtained either **a**, from simulation or **b**, from fitting the data obtained from time-resolved fluorescence (right, adapted from ref.[34]) monitoring the excitation energy flow in the PBS. In simulations, PBS was excited into the far end of the rod. The ~100 ps component (green) in the experimental data was interpreted as due to excitation annihilation[35], hence it is not present in the simulation. **c**, PBS arrays were modeled based on cryo-electron tomography data from ref.[40]. a, only the up-up conformation is compatible with PBS arrays. **d**, The up-down conformation would result in array termination**. e**, A PBS switching to the down-down conformation could result in array dispersion.*

39

References

582

583 1 Sanchez-Baracaldo, P., Bianchini, G., Wilson, J. D. & Knoll, A. H. Cyanobacteria and biogeochemical cycles through Earth history. *Trends Microbiol*, doi:10.1016/j.tim.2021.05.008 (2021).

586 2 Kumar, J., Singh, D., Tyagi, M. B. & Kumar, A. Cyanobacteria: Applications in Biotechnology. *Cyanobacteria: From Basic Science to Applications*, 327-346, doi:10.1016/B978-0-12-814667-5.00016-7 (2019).

589 3 Gantt, E. & Conti, S. F. Phycobiliprotein localization in algae. *Brookhaven Symp Biol* **19**, 393-405 (1966).

591 4 Gantt, E. & Conti, S. F. Granules associated with the chloroplast lamellae of Porphyridium cruentum. *J Cell Biol* **29**, 423-434, doi:10.1083/jcb.29.3.423 (1966).

593 5 Tandeau de Marsac, N. Phycobiliproteins and phycobilisomes: the early observations. *Photosynth Res* **76**, 193-205, doi:10.1023/A:1024954911473 (2003).

595 6 Grossman, A. R., Schaefer, M. R., Chiang, G. G. & Collier, J. L. The phycobilisome, a light-harvesting complex responsive to environmental conditions. *Microbiol Rev* **57**, 725-749, doi:10.1128/mr.57.3.725-749.1993 (1993).

598 7 de Marsac, N. T. & Cohen-bazire, G. Molecular composition of cyanobacterial phycobilisomes. *Proc Natl Acad Sci U S A* **74**, 1635-1639, doi:10.1073/pnas.74.4.1635 (1977).

600 8 Adir, N. Elucidation of the molecular structures of components of the phycobilisome: reconstructing a giant. *Photosynth Res* **85**, 15-32, doi:10.1007/s11120-004-2143-y (2005).

602 9 Glauser, M. *et al.* Phycobilisome structure in the cyanobacteria Mastigocladus laminosus and Anabaena sp. PCC 7120. *Eur J Biochem* **205**, 907-915, doi:10.1111/j.1432-1033.1992.tb16857.x (1992).

605 10 Ducret, A., Sidler, W., Wehrli, E., Frank, G. & Zuber, H. Isolation, characterization and electron microscopy analysis of a hemidiscoidal phycobilisome type from the cyanobacterium Anabaena sp. PCC 7120. *Eur J Biochem* **236**, 1010-1024, doi:10.1111/j.1432-1033.1996.01010.x (1996).

609 11 Ducret, A. *et al.* Reconstitution, characterisation and mass analysis of the pentacylindrical allophycocyanin core complex from the cyanobacterium Anabaena sp. PCC 7120. *J Mol Biol* **278**, 369-388, doi:10.1006/jmbi.1998.1678 (1998).

612 12 Anderson, L. K. & Toole, C. M. A model for early events in the assembly pathway of cyanobacterial phycobilisomes. *Mol Microbiol* **30**, 467-474, doi:10.1046/j.1365-2958.1998.01081.x (1998).

615 13 Schirmer, T., Bode, W. & Huber, R. Refined three-dimensional structures of two cyanobacterial C-phycocyanins at 2.1 and 2.5 A resolution. A common principle of phycobilin-protein interaction. *J Mol Biol* **196**, 677-695, doi:10.1016/0022-2836(87)90040-4 (1987).

618 14 Schirmer, T. *et al.* Crystal structure analysis and refinement at 2.5 A of hexameric C-phycocyanin from the cyanobacterium Agmenellum quadruplicatum. The molecular model and its implications for light-harvesting. *J Mol Biol* **188**, 651-676, doi:10.1016/s0022-2836(86)80013-4 (1986).

622 15 Zhang, J. *et al.* Structure of phycobilisome from the red alga Griffithsia pacifica. *Nature* **551**, 57-63, doi:10.1038/nature24278 (2017).

624 16 Ma, J. *et al.* Structural basis of energy transfer in Porphyridium purpureum phycobilisome. *Nature* **579**, 146-151, doi:10.1038/s41586-020-2020-7 (2020).

626 17   Zheng, L. *et al.* Structural insight into the mechanism of energy transfer in cyanobacterial
627   phycobilisomes. *Nat Commun* **12**, 5497, doi:10.1038/s41467-021-25813-y (2021).
628 18   MacColl, R. Cyanobacterial phycobilisomes. *J Struct Biol* **124**, 311-334,
629   doi:10.1006/jsbi.1998.4062 (1998).
630 19   Glazer, A. N. Light guides. Directional energy transfer in a photosynthetic antenna. *J Biol Chem*
631   **264**, 1-4 (1989).
632 20   Gantt, E. & Lipschultz, C. A. Phycobilisomes of Porphyridium cruentum. I. Isolation. *J Cell Biol*
633   **54**, 313-324, doi:10.1083/jcb.54.2.313 (1972).
634 21   Arteni, A. A. *et al.* Structure and organization of phycobilisomes on membranes of the red
635   alga Porphyridium cruentum. *Photosynth Res* **95**, 169-174, doi:10.1007/s11120-007-9264-z
636   (2008).
637 22   Arteni, A. A., Ajlani, G. & Boekema, E. J. Structural organisation of phycobilisomes from
638   Synechocystis sp. strain PCC6803 and their interaction with the membrane. *Biochim Biophys*
639   *Acta* **1787**, 272-279, doi:10.1016/j.bbabio.2009.01.009 (2009).
640 23   Williams, R. C., Gingrich, J. C. & Glazer, A. N. Cyanobacterial phycobilisomes. Particles from
641   Synechocystis 6701 and two pigment mutants. *J Cell Biol* **85**, 558-566,
642   doi:10.1083/jcb.85.3.558 (1980).
643 24   Yamanaka, G., Glazer, A. N. & Williams, R. C. Molecular architecture of a light-harvesting
644   antenna. Comparison of wild type and mutant Synechococcus 6301 phycobilisomes. *J Biol*
645   *Chem* **255**, 11104-11110 (1980).
646 25   Chang, L. *et al.* Structural organization of an intact phycobilisome and its association with
647   photosystem II. *Cell Res* **25**, 726-737, doi:10.1038/cr.2015.59 (2015).
648 26   Guglielmi, G., Cohenbazire, G. & Bryant, D. A. The Structure of Gloeobacter-Violaceus and Its
649   Phycobilisomes. *Arch Microbiol* **129**, 181-189, doi:Doi 10.1007/Bf00425248 (1981).
650 27   Mills, L. A., McCormick, A. J. & Lea-Smith, D. J. Current knowledge and recent advances in
651   understanding metabolism of the model cyanobacterium Synechocystis sp. PCC 6803. *Biosci*
652   *Rep* **40**, doi:10.1042/BSR20193325 (2020).
653 28   Adir, N., Bar-Zvi, S. & Harris, D. The amazing phycobilisome. *Biochim Biophys Acta Bioenerg*
654   **1861**, 148047, doi:10.1016/j.bbabio.2019.07.002 (2020).
655 29   Liu, H. *et al.* Structure of cyanobacterial phycobilisome core revealed by structural modeling
656   and chemical cross-linking. *Sci Adv* **7**, doi:10.1126/sciadv.aba5743 (2021).
657 30   Han, B. G. *et al.* Long shelf-life streptavidin support-films suitable for electron microscopy of
658   biological macromolecules. *J Struct Biol* **195**, 238-244, doi:10.1016/j.jsb.2016.06.009 (2016).
659 31   Mullineaux, C. W. Phycobilisome-reaction centre interaction in cyanobacteria. *Photosynthesis*
660   *Research* **95**, 175-182, doi:10.1007/s11120-007-9249-y (2008).
661 32   Calzadilla, P. I., Muzzopappa, F., Setif, P. & Kirilovsky, D. Different roles for ApcD and ApcF in
662   Synechococcus elongatus and Synechocystis sp. PCC 6803 phycobilisomes. *Biochim Biophys*
663   *Acta Bioenerg* **1860**, 488-498, doi:10.1016/j.bbabio.2019.04.004 (2019).
664 33   Dong, C. *et al.* ApcD is necessary for efficient energy transfer from phycobilisomes to
665   photosystem I and helps to prevent photoinhibition in the cyanobacterium Synechococcus
666   sp. PCC 7002. *Biochim Biophys Acta* **1787**, 1122-1128, doi:10.1016/j.bbabio.2009.04.007
667   (2009).
668 34   Tian, L. *et al.* Picosecond kinetics of light harvesting and photoprotective quenching in wild-
669   type and mutant phycobilisomes isolated from the cyanobacterium Synechocystis PCC 6803.
670   *Biophys J* **102**, 1692-1700, doi:10.1016/j.bpj.2012.03.008 (2012).
671 35   van Stokkum, I. H. M. *et al.* A functional compartmental model of the Synechocystis PCC 6803
672   phycobilisome. *Photosynth Res* **135**, 87-102, doi:10.1007/s11120-017-0424-5 (2018).

673 36 Xie, M. *et al.* Difference in light use strategy in red alga between Griffithsia pacifica and
674   Porphyridium purpureum. *Sci Rep* **11**, 14367, doi:10.1038/s41598-021-93696-6 (2021).
675 37 Kruger, T. P. J., van Grondelle, R. & Gwizdala, M. The role of far-red spectral states in the
676   energy regulation of phycobilisomes. *Biochim Biophys Acta Bioenerg* **1860**, 341-349,
677   doi:10.1016/j.bbabio.2019.01.007 (2019).
678 38 Glazer, A. N., Lundell, D. J., Yamanaka, G. & Williams, R. C. The structure of a "simple"
679   phycobilisome. *Ann Microbiol (Paris)* **134B**, 159-180, doi:10.1016/s0769-2609(83)80103-3
680   (1983).
681 39 Liu, H. *et al.* Phycobilisomes supply excitations to both photosystems in a megacomplex in
682   cyanobacteria. *Science* **342**, 1104-1107, doi:10.1126/science.1242321 (2013).
683 40 Rast, A. *et al.* Biogenic regions of cyanobacterial thylakoids form contact sites with the plasma
684   membrane. *Nat Plants* **5**, 436-446, doi:10.1038/s41477-019-0399-7 (2019).
685 41 Dominguez-Martin, M. A. *et al.* Structure of the quenched cyanobacterial OCP-phycobilisome
686   complex. *Submitted*.
687 42 Araoz, R. & Hader, D. P. Ultraviolet radiation induces both degradation and synthesis of
688   phycobilisomes in Nostoc sp.: a spectroscopic and biochemical approach. *Fems Microbiol Ecol*
689   **23**, 301-313, doi:10.1111/j.1574-6941.1997.tb00411.x (1997).
690 43 Gantt, E., Lipschultz, C. A., Grabowski, J. & Zimmerman, B. K. Phycobilisomes from blue-green
691   and red algae: isolation criteria and dissociation characteristics. *Plant Physiol* **63**, 615-620,
692   doi:10.1104/pp.63.4.615 (1979).
693 44 Tivol, W. F., Briegel, A. & Jensen, G. J. An improved cryogen for plunge freezing. *Microsc*
694   *Microanal* **14**, 375-379, doi:10.1017/S1431927608080781 (2008).
695 45 Schorb, M., Haberbosch, I., Hagen, W. J. H., Schwab, Y. & Mastronarde, D. N. Software tools
696   for   automated   transmission   electron   microscopy.   *Nat Methods* **16**, 471-477,
697   doi:10.1038/s41592-019-0396-9 (2019).
698 46 Sun, M. *et al.* Practical considerations for using K3 cameras in CDS mode for high-resolution
699   and   high-throughput   single   particle   cryo-EM. *J Struct Biol* **213**, 107745,
700   doi:10.1016/j.jsb.2021.107745 (2021).
701 47 Scheres, S. H. RELION: implementation of a Bayesian approach to cryo-EM structure
702   determination. *J Struct Biol* **180**, 519-530, doi:10.1016/j.jsb.2012.09.006 (2012).
703 48 Punjani, A., Rubinstein, J. L., Fleet, D. J. & Brubaker, M. A. cryoSPARC: algorithms for rapid
704   unsupervised   cryo-EM   structure   determination.   *Nat Methods* **14**, 290-296,
705   doi:10.1038/nmeth.4169 (2017).
706 49 Rosenthal, P. B. & Henderson, R. Optimal determination of particle orientation, absolute
707   hand, and contrast loss in single-particle electron cryomicroscopy. *J Mol Biol* **333**, 721-745,
708   doi:10.1016/j.jmb.2003.07.013 (2003).
709 50 Sanchez-Garcia, R. *et al.* DeepEMhancer: a deep learning solution for cryo-EM volume post-
710   processing. *Commun Biol* **4**, 874, doi:10.1038/s42003-021-02399-1 (2021).
711 51 Liebschner, D. *et al.* Macromolecular structure determination using X-rays, neutrons and
712   electrons: recent developments in Phenix. *Acta Crystallogr D Struct Biol* **75**, 861-877,
713   doi:10.1107/S2059798319011471 (2019).
714 52 Shevchenko, A., Wilm, M., Vorm, O. & Mann, M. Mass spectrometric sequencing of proteins
715   silver-stained polyacrylamide gels. *Anal Chem* **68**, 850-858, doi:10.1021/ac950914h (1996).
716 53 Pullerits, T., Hess, S., Herek, J. L. & Sundstrom, V. Temperature dependence of excitation
717   transfer in LH2 of Rhodobacter sphaeroides. *Journal of Physical Chemistry B* **101**, 10560-
718   10567, doi:DOI 10.1021/jp9720956 (1997).

719   54   Sauer, K. & Scheer, H. Excitation Transfer in C-Phycocyanin - Forster Transfer Rate and Exciton
720   Calculations Based on New Crystal-Structure Data for C-Phycocyanins from Agmenellum-
721   Quadruplicatum and Mastigocladus-Laminosus. *Biochimica Et Biophysica Acta* **936**, 157-170,
722   doi:Doi 10.1016/0005-2728(88)90232-0 (1988).

723   55   Demidov, A. A. & Mimuro, M. Deconvolution of C-phycocyanin beta-84 and beta-155
724   chromophore absorption and fluorescence spectra of cyanobacterium Mastigocladus
725   laminosus. *Biophys J* **68**, 1500-1506, doi:10.1016/S0006-3495(95)80322-X (1995).

726   56   Fuente, D., Lazar, D., Oliver-Villanueva, J. V. & Urchueguia, J. F. Reconstruction of the
727   absorption spectrum of Synechocystis sp. PCC 6803 optical mutants from the in vivo signature
728   of individual pigments. *Photosynth Res* **147**, 75-90, doi:10.1007/s11120-020-00799-8 (2021).

729   57   Squires, A. H. & Moerner, W. E. Direct single-molecule measurements of phycocyanobilin
730   photophysics in monomeric C-phycocyanin. *Proc Natl Acad Sci U S A* **114**, 9779-9784,
731   doi:10.1073/pnas.1705435114 (2017).

732   58   Larkin, M. A. *et al.* Clustal W and Clustal X version 2.0. *Bioinformatics* **23**, 2947-2948,
733   doi:10.1093/bioinformatics/btm404 (2007).

734   59   Kozlov, A. M., Darriba, D., Flouri, T., Morel, B. & Stamatakis, A. RAxML-NG: a fast, scalable and
735   user-friendly tool for maximum likelihood phylogenetic inference. *Bioinformatics* **35**, 4453-
736   4455, doi:10.1093/bioinformatics/btz305 (2019).

737   60   Capella-Gutierrez, S., Silla-Martinez, J. M. & Gabaldon, T. trimAl: a tool for automated
738   alignment trimming in large-scale phylogenetic analyses. *Bioinformatics* **25**, 1972-1973,
739   doi:10.1093/bioinformatics/btp348 (2009).

740   61   Crooks, G. E., Hon, G., Chandonia, J. M. & Brenner, S. E. WebLogo: a sequence logo generator.
741   *Genome Res* **14**, 1188-1190, doi:10.1101/gr.849004 (2004).

742   62   Goddard, T. D. *et al.* UCSF ChimeraX: Meeting modern challenges in visualization and analysis.
743   *Protein Sci* **27**, 14-25, doi:10.1002/pro.3235 (2018).